Shiva, A., Sadati, S. M. H., Noh, Y., Fraś, J., Ataka, A., Würdemann, H., Hauser, H., Walker, I. D., Nanayakkara, T., & Althoefer, K. (2019). Elasticity Versus Hyperelasticity Considerations in Quasistatic Modeling of a Soft Finger-Like Robotic Appendage for Real-Time Position and Force Estimation. *Soft Robotics*, *6*(2), 228-249. https://doi.org/10.1089/soro.2018.0060

Elasticity vs. Hyperelasticity Considerations in Quasi-Static Modelling of a Soft Finger-like Robotic Appendage for Real-time Position & Force Estimation

A. Shiva[1,2], S.M.H. Sadati[2,5], Y. Noh[1], J. Fraś[3,4], A. Ataka[1,3], H. Wurdemann[6], H. Hauser[5], I. Walker[7], T. Nanayakkara[2], K. Althoefer[3]

[1]Centre for Robotics Research, King's College London, London WC2R 2LS, UK. (Corresponding Author: ali.shiva@kcl.ac.uk) ({yohan.noh , ahmad_ataka_awwalur.rizqi }@kcl.ac.uk)
[2]Dyson School of Design Eng., Imperial College London, London SW7 1NA, UK. (t.nanayakkara@imperial.ac.uk)
[3]Advanced Robotics @ Queen Mary (ARQ), Queen Mary University of London, London E1 4NS, UK. ({j.fras , k.althoefer}@qmul.ac.uk)
[4]Industrial Research Institute for Automation and Measurements PIAP, 02-486 Warsaw, Poland.
[5]Faculty of Eng., University of Bristol, BS8 1TH, UK. ({s.m.hadi.sadati , helmut.hauser}@bristol.ac.uk)
[6]Dept. of Mechanical Eng., University College London, London WC1E 7JE, UK. (h.wurdemann@ucl.ac.uk)
[7]Dept. of Electrical & Computer Eng., Clemson University, Clemson, SC 29634, USA. (iwalker@clemson.edu)

Abstract — Various methods based on hyperelastic assumptions have been developed to address the mathematical complexities of modelling motion and deformation of continuum manipulators. Here, we propose a quasi-static approach for 3D modelling and real-time simulation of a pneumatically actuated soft continuum robotic appendage to estimate the contact forces and the overall pose. Our model can incorporate external load at any arbitrary point on the body and deliver positional and force propagation information along the entire backbone. In line with the proposed model, the effectiveness of elasticity vs. hyperelasticity assumptions (Neo-Hookean and Gent) are investigated and compared. Experiments are carried out with and without external load, and simulations are validated across a range of Young's moduli. Results show best conformity with Hooke's model for limited strains with about 6% average normalized error of position; and a mean absolute error of less than 0.08N for force applied at the tip and on the body; demonstrating high accuracy in estimating the position and the contact forces.

1. INTRODUCTION

Qualities such as dexterity and high deformability in biological appendages like the octopus arm has sparked a research trend which aims to replicate these features using intrinsically soft materials in continuum robotic platforms; with the promise of safely performing delicate tasks [1] [2], improving maneuverability in confined or unstructured environments [3], achieving higher dexterity for grasping [4] [5] or for motion in dynamic biomimetic systems [6] [7] such as submerged locomotion [8] [9]. These robots are also appealing for investigating morphological computation [10] and embodied intelligence [8], providing a framework for bodily force sensing without the need for additional sensory hardware, in contrast to rigid-link robots [11].

Yet, the inherent structural flexibility results in modelling and/or control [12] challenges. Several approaches have been investigated for modelling this class of manipulators. Beyond the distinction between planar (2D) [4] [11] [13] [14] [15] [16] or spatial (3D) [17] [18] [19] [20] [21] operation, it seems plausible to identify two key stages which determine the modelling strategy:

I. The "Priori" stage; to consider:
   - Taking external loading into account vs. no external loads; and,
   - Inertial (dynamic) vs. non-inertial (static/quasi-static, or kinematic) modelling.

II. The "Approach" stage; to consider a mechanistic solution vs. shape function estimation (or a combination). While the former might entail some experimental identification, yet is based on

analytical derivation and solving of the mechanistic equations, with the potential to be more comprehensive. The latter, on the other hand, is entirely structure-specific in implementation; with the unknown coefficients to be determined from the manipulator's behavior.

The constant curvature (CC) formulation has widely been employed (e.g.[13 17 22 23 24 25 26]) for mapping the actuation space to the configuration space by formulating the backbone deformation as a planar curve with constant radius. In this regard, Webster and Jones [27] demonstrate two separate sub-mappings: a robot-specific map relating the mechanical actuation to the three arc parameters (Fig.2), and a robot-agnostic map relating the arc parameters to the spatial kinematic configuration of the manipulator. The first mapping usually involves some identification of the system from experiments; e.g. as in Chen et al. [22], where a CC model is developed to control the manipulator's shape via tip position control.

However, the validity of CC depends on the mechanical and geometrical properties of the structure and/or the magnitude of loads. For example, torsional effects are reported to be capable of significant effects on the behavior and deformation of soft manipulators [28] which CC falls short of incorporating [29]; in addition to shear or internal forces [30] when resulting in deformations not conforming to a curve.

Conversely, variable curvature (VC) methods offer more viable solutions in the presence of external loads, in addition to providing singularity-free kinematic maps [31 32 33]. Many research works achieve VC from CC by modifications, such as deviations added as uncertainty [34], piecewise CC (PCC) [19 27 35] such as a serial chain of subsegment arcs [36], PCC along with a compensating free parameter (identified experimentally) [37], PCC combined with general 3D paths described by B-spline curves [20], PCC with internal friction forces [38], or Piecewise Constant Strain (PCS) modelling based on screw theory [35].

As an alternative approach to VC methods, approximate identification based on polynomial solutions for estimating the shape function have been proposed [39 40 41], where the coefficients are identified using experimental results to derive a structure-specific model. Godage et al. [39] use a horizontally fixed orientation to train the coefficient matrices to derive a solution-based model for the kinematic map and implement the identified solution in the Lagrange equations of motion; however this is achieved without considering external loads. Their model is singularity free and accurate w.r.t the training data sets, and the final solution is faster than beam modelling and lumped parameter methods.

Although identification based models are relatively accurate, computationally efficient, and appropriate for real-time control [42], their validity is limited to their experimentally-derived conditions, presence and/or magnitude of external loads, input values and training data sets; and do not account for the structural characteristics. Results are not guaranteed when dealing with unknown conditions, and are not intuitive for shape interpretation [32].

In this regard, Beam Theory [3 13 17 43 44 45] (such as Euler-Bernoulli models with small deflections in the absence of shear [14 37 45 47]) and Cosserat rods [18 20 21 29 31 46] have been considered. Beam modelling has also been applied as infinitesimal elements along the body [48] similar to the infinitesimal CC elements to attain VC kinematics. For a tendon-driven catheter, Rucker and Webster [21] couple Cosserat string and Cosserat rod models for the tendons and the backbone respectively, by deriving the distributed loads on the backbone from the tendons and solving via numerical integration. Shear and extension are considered negligible hence omitted. Their model was adopted by Neumann et al. [20] in a 3D follow-the-leader scenario with distributed loads from self-weight, and applied to their tendon-driven setup (assumed to be frictionless) for beam statics and dynamics. After predicting a CC path, the true response is optimized, yielding a solution incorporating bending, shear, and extension; resulting in a VC solution with a robot-specific mechanical map which is free from singularity. Godage et al. [33] implemented the Cosserat rod model for a multi-section continuum arm, resulting in a boundary value problem (BVP) with a system of non-linear equations to be solved using recursive numerical optimization; however in the absence of external loads. As a drawback, Sadati et al. [42] note in a comparative study that Cosserat rod models entail relatively cumbersome calculations which could be a hindrance.

In the modelling approach presented in this paper, we take three key elements into consideration:

A. Discrete Kinematics

Various structures for continuum manipulators have been designed to emulate continuum articulation along the entire body. Thus, many of the continuum manipulators are developed as serially concatenated multi-segment (e.g. [1 8 17 31 49 50]) or as multi-section robots (e.g. [26 39 51 46 52]). This type of design makes discrete modelling appealing [15 33 48 53]. A well-known method to this end is the lumped parameter approach which approximates the continuum embodiment with a series of rigid-link segments interconnected via compliant joints [15 30 51 54 55], or in a network of spring-mass-damper [49], or in conjunction with other methods such as virtual power [36]. For example, Godage et al. [55] implemented Lagrangian dynamics for a lumped model to achieve VC kinematics, yet assuming that the robot always deforms in a circular arc without twisting. Tatlicioglu et al. [15] employed lumped modelling to capture the planar behavior of the three section OctArm where the total kinetic energy is computed for an infinite number of rigid sections, and the summation over the Lagrangian terms is replaced with an integral over the backbone handing continuum Lagrange dynamics, albeit without torsion. However, while lumped parameter models reduce complexity of analysis, they are considered to be less accurate [55] and usually suffer from extensive calculations [32].

Alternatively, discretized differential equation describing variable curvature kinematics can be used for forward integration of a model with finite number of elements (FEM) [56 57 58]. Here, the main difference in modeling assumptions with the lumped system approach (also consisting of finite number of segments) is that the manipulator kinematics is not based on series link rigid body kinematics. Both models eliminate spatial integration, by considering a finite number of kinematic states associated with each element and result in a large and computationally expensive system of equations, usually expressed in vector format. FEM models, however, are overwhelmingly restricted to off-line structural analysis and optimization rather than system modeling for control purposes[56]. Real-time FEM based solutions for continuum manipulator mechanics and control have been extensively studied by Duriez et al., by utilizing mass matrix sparsity in the resulting system of equations [56 57]. This sparsity is not achievable with series-link rigid body kinematics approach where relative states (e.g. joint angular and transnational position) are usually considered as the modeling states rather than element absolute states (e.g. element orientation and position w.r.t. the reference frame). Moreover, reports on real-time implementation of this method mention execution cycles of less than 40Hz [59].

B. Quasi-static vs. Dynamic Modelling

While many dynamic models have been proposed (e.g. [6 21 31 33 51 61]), nonetheless with most continuum manipulators, inertial effects due to motion could be neglected by assuming static equilibrium and slow transitions in the system states [32], as they are not operated close to dynamic boundaries [51]. Besides, silicon-based continuum manipulators present under-damped nonlinear dynamic modes with relatively large-value nonlinear damping and short transition time [62]. While the transition time is insignificant and fast in most applications, capturing their exact behavior requires extensive analytical and computational efforts [41].

Hence, static [18 34 37 44], quasi-static [11 16 45 47 63], and kinematic analyses [25 34 38] are deemed as reasonable assumptions for kinematic modelling and force sensing. Such circumstances are frequently witnessed in medical interventions [2 8 64] such as Minimally Invasive Surgery [1 28 65 66], catheterization [13 17 23], bladder surveillance [67], colonoscopy [22], endoscopic surgery [38], or other areas in medical training [68]. The same is true for most proposed assistive tasks [19 69 70], for example using bionic hands [26]. This assumption has also been employed in motion control [23 71], navigation [53 72], path following [52], leader following [20], manipulation [47 73 53], grasping [25 53], or realizing biomimetic systems [68]. Even when developing a lumped model for a catheter, Jung et. al. [30] claim that the dynamics of the system is not a significant factor and is only considered to incorporate nonlinear friction, as they solve for the quasi-static solution. Shapiro et. al. [45] implement a quasi-static kinematic model using an iterative solver for a simple Euler–Bernoulli (EB) beam model using CC for kinematic maps in a bi-bellows manipulator. The STIFF-FLOP manipulator [1 74] is modelled by Fraś et al. [48] in a quasi-static approach but without shear. Tunay [60]

developed a spatial model using quaternions for the configurational variables of the Cosserat rod model and solves for bending, twisting, extension, and shear via approximate series solution for static modeling for the weak-form integral equations in a finite element discretized form. This approach is accurate and comprehensive, but with a complex shape function and limitations related to the finite element method. Xu & Simaan [75] analyzed static equilibrium using elliptic integrals in a multi-backbone robot to investigate 2 DoF bending. A quasi-static EB beam analysis is employed by Alici et al. [47] to formulate the 2D bending behavior of an arm of a silicon gripper.

Moreover, as force measurement and control plays a crucial role in human robot interaction, many of the inertia-less models have been used for force sensing [11 28 34 76]; e.g., Bajo & Simaan [71] developed a motion/force control algorithm assuming interaction forces (applied specifically at the tip) do not deform the continuum manipulator beyond circular bending for the segments. A deflection based force sensing algorithm is presented in [46] which utilizes Kalman filtering in a probabilistic approach to estimate forces applied at the tip. An intrinsic force sensing method is proposed in [64] to sense the wrench applied at the tip of continuum robot with 2 DoF bending motion.

C. Elasticity vs. Hyperelasticity

Low-modulus materials are favorable candidates for the core structure as they enable reduction of actuation forces; which, in addition to biocompatibility [77] and safety [78], have made elastomers such as silicon a popular choice for the body. In this regard, silicon has been used not only with tendons (as actuators) [6 14 44 79], but extensively in manipulators which entail actuators operating on the principle of fluidic expansion in chambers reinforced with inextensible fibers [80], constituting braided extensors (e.g. [1 22 28 65 73 81]), or fiber-reinforced bending actuators [16], or hybrid actuation [49 82]. Hence, hyperelastic modelling, using Neo-Hookean [11 16 32 31] or Yeoh [11] formulation has received attention for soft component modelling, e.g. braided pneumatic actuators. Trivedi et. al. [31] applied the principle of virtual work to derive elongation for the braided extensor assuming Neo-Hookean behavior and use a Cosserat rod model resulting in a boundary value problem (BVP), solving non-linear equations via numerical methods to achieve VC kinematics for the planar 2D motion assuming infinite shear. Sadati et al. [32] proposed a geometry deformation model employing PCC, where the bending of a braided pneumatic actuator is studied along with the effect of cross-section deformation and is compared to experimental results, entailing a method which is mathematically intensive.

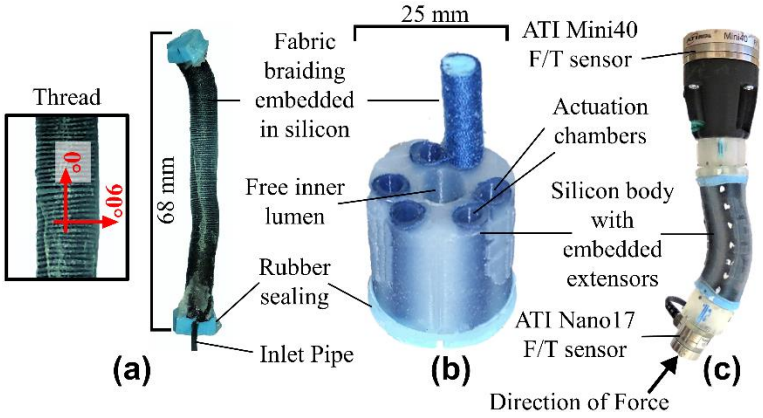

Fig.1: (a) A single braided extensor; elongated due to pressurization via inlet air pipe; with the thread angle shown (b) Cutaway of the body with one of the braided extensors (fluidic elastomer actuators) kept intact. (c) STIFF-FLOP manipulator; with ATI Nano17 and ATI Mini40 force sensors at the tip and base, respectively; and pressurized while applying force at the tip sensor.

2. OBJECTIVES & CONTRIBUTIONS

Following on from our earlier works [32 42], for a pneumatic soft continuum robotic appendage comprising braided extensors, we propose a forward kinematics (FK), quasi-static, discrete VC model for real-time

contact force sensing. Our approach accounts for shear, torsion, bending and extension; with its validity not restricted to training data. The model is spatial (3D) and computationally efficient for real-time simulation of position and deformation. In line with facilitating contact-force sensing, the external force can be applied at theoretically any arbitrary point on the body and not only at the tip, thus being practically beneficial for sensor-deprived environments and soft tactile sensing. Position and force information propagate toward the proximal base and are retrievable at any selected point along the backbone via discretization (based on a number of sections definable by the user). Structural inhomogeneity such as rigid inter-segment connective elements can be included. Our approach is capable of reporting back on the pressure values from actuation, which is desirable for control strategies.

The real-time discretized approach allows us to include and exploit local information, in the form of internal constraints on the physical structure via the infinitesimal segments. Basically, rather than having "clean" equations via a closed form approach, we "open up" the system to calculate the internal effects - but still get the same basic shapes and movements as generated by alternative approaches such as those obtained from beam theory. Our approach, inherently computes internal forces/strains that, in canceling out between the segments, do not directly cause motion, but do contribute to the mechanical stress imposed on the structure, enabling real-time monitoring of the health of the system.

The main contributions of this work are summarized as follows:

1. Developing a model for real-time contact force estimation, based on discrete VC that benefits from simple forward spatial integration, capable of handling external and body loads, and estimating contact force at the tip or on any arbitrary point on the body.

2. Investigating the validity of elasticity compared to the conventionally-used hyperelastic methods, and analyzing whether the added complexity due to hyperelastic assumptions would assist the accuracy of continuum actuator modules comprising braided extensors in such robotic platforms where only limited strains are produced.

3. MATERIALS AND METHODS

A. Physical Structure

The soft robotic appendage developed in the EU FP7 project STIFF-FLOP is a cylinder of silicon (Ecoflex-0050, Smooth-on Inc.) with an overall length of 47mm, outer diameter of 25mm and inner diameter of 9mm. Embedded in the cylinder wall are three pairs of braided extensors (fiber-reinforced pressure chambers); aligned with the cylinder's longitudinal axis and mutually oriented at 120° from each other (Fig.1). Each pair of braided extensors is pneumatically actuated via a 2mm outer diameter inlet air pipe; independent of the other two chamber pairs and therefore enabling the manipulator to bend by varying the air pressure in one chamber pair relative to the other two. Simultaneous pressurization of the all chamber pairs elongates the manipulator. The central lumen enables the passing through of necessary actuation tubes in case of serially assembling multiple segments. A rigid hollow attachment of 3D-printed material is affixed at the tip for sensor connection. A more detailed description of the STIFF-FLOP manipulator is given in [1] [74].

B. Modelling Framework

The following assumptions are made throughout our approach:

1- Manipulator cross-sections remain circular [13] [55].
2- Gravitational forces are ignored (verified in millimeter size continuum manipulators [11] [30] [64]) with no noticeable effect on the results for the given setup and experiments.
3- The chamber shell volume is constrained by the fiber braiding during its deformation [32].
4- PCC assumption is used only to calculate the incremental bending component between each pair of neighboring infinitesimally-distanced frames.

B.1- Pneumatic Braided Extensors

The intrinsic actuation of the robotic appendage is achieved via the braided extensors, which consist of silicone walls reinforced with fiber threads (Fig.1(c)). Poisson's ratio (denoted by ν) is 0.499 for elastomers [83]; which given the relation between Young's modulus (E) and the shear modulus (G) as: $E = 2G(1+\nu)$, results in $E = 3G$; indicating incompressible isotropic material. Hence, the principal engineering stresses for each braided extensor are calculated by [16]:

$$\sigma_j = \frac{\partial u}{\partial \lambda_j} - p\lambda_j^{-1}\,, j = 1,2,3 \tag{1}$$

where u is the deformation energy density, p is the Lagrange multiplier, and the λ_j's are the Cauchy-Green principal stretches constituting the first invariant of the right Cauchy-Green deformation tensor as: $I_1 = \sum_{j=1}^{3} \lambda_j^2$. Incompressibility yields: $\lambda_1\lambda_2\lambda_3 = 1$. Alternatively, the longitudinal stress in each braided extensor can be expressed as a function of internal pressure P and axial forces as:

$$\sigma = P\, r_n^2/(r_o^2 - r_n^2) + f_z \tag{2}$$

denoting the outer and inner radii as r_o and r_n respectively, and the resultant boundary axial force as f_z (setting local z axis in chamber's axial direction). The volume of the chamber wall is: $V_t = \pi(r_o^2 - r_n^2)l_1$, and volume of the area pressurized by air is: $V_{ch} = \pi r_n^2 \lambda_2^2 l_1 \lambda_1$, where $l_2 = \lambda_1 l_1$ and $r_2 = \lambda_2 r_{o,n}$ are the deformed length and radii (outer or inner), respectively. For utilizing the Principle of Virtual Work, it is noted that the total deformation action is calculated by: $U = u.V_t$. The total action of the actuation medium (air) is: $W = P.V_{ch}$. For a 3D distributed energy field in equilibrium, we can write:

$$\delta W = \delta U \tag{3}$$

Solving this equation results in the expression of stress as a function of the elongation, depending on the deformation energy density function as well as the chosen constraint for the Lagrange multiplier. We comparatively investigate three modelling frameworks:

1. Hookean (H): Each extensor is assumed to elongate according to Hooke's law,
$$\lambda_1 = (\sigma/E) + 1 \tag{4}$$
2. Neo-Hookean (NH): One of the most representative strain energy density mechanistic functions in this class [84] which is derived based on the underlying material structure,
$$u = E(I_1 - 3)/6 \tag{5}$$
3. Gent (G): A hybrid empirical/mechanistic yet mathematically simple model, which captures the strain-stiffening at large strains observed experimentally [85],
$$u = -\left(\frac{G}{2}\right) J_m \ln[1 - (I_1 - 3)/J_m] \tag{6}$$
where J_m is the constant value for limiting polymeric chain extensibility [85] such that: $J_m + 3 = \lambda_m^2 + (2/\lambda_m)$ [83]. For Ecoflex-0050, $\lambda_m = 9.8$ results in: $J_m = 93.2$.

For the two hyperelastic models (NH and G) we investigate three types of constraints to solve Eqn.(1):

A. Uniaxial extension (UNI); where $\lambda_1 = \lambda, \lambda_2 = \lambda_3 = {}^{1}/_{\sqrt{\lambda}}$.
B. Inextensible fiber (INF); where $\lambda_1^2 C_\gamma^2 + \lambda_2^2 S_\gamma^2 = 1$, and $\gamma \in (0, \pi/2)$ is the braiding angle [80] (C_γ and S_γ represent $\cos\gamma$ and $\sin\gamma$ respectively).
C. No radial deformation (NR); where $\lambda_1 = \lambda, \lambda_2 = 1, \lambda_3 = {}^{1}/_{\lambda}$. It should be noted that this case is the simplified version of the previous case where the braiding angle is 90° which is valid for a dense braiding [16 32 42].

The Neo-Hookean (NH) model with Constraints:

Uniaxial extension (NH-UNI): The engineering stress is calculated as: $\sigma = G(\lambda - {}^{1}/_{\lambda^2})$. The relation is rearranged to: $\lambda^3 - (\sigma/G)\lambda^2 - 1 = 0$; and solved for λ using the cubic equation as:

$$\lambda = \left[\frac{\sigma^3}{27G^3} - \left(\left[\left(\frac{\sigma^3}{27G^3} + \frac{1}{2}\right)^2 - \frac{\sigma^6}{729G^6}\right]^{\frac{1}{2}} + \frac{1}{2}\right]^{\frac{1}{3}} + \left[\frac{\sigma^3}{27G^3} + \left(\left[\left(\frac{\sigma^3}{27G^3} + \frac{1}{2}\right)^2 - \frac{\sigma^6}{729G^6}\right]^{\frac{1}{2}} + \frac{1}{2}\right]^{\frac{1}{3}} + \frac{\sigma}{3G}\right. \tag{7}$$

Inextensible fiber (NH-INF): The engineering stress is calculated as:

$$\sigma = 2G(1-\lambda^2)\left[\begin{matrix}(1 - 2S_\gamma^6 + 5S_\gamma^4 - 4S_\gamma^2)\lambda^6 + (7S_\gamma^6 - 16S_\gamma^4 + 11S_\gamma^2 - 2)\lambda^4 + \\ (7S_\gamma^6 - 4S_\gamma^4 - 3S_\gamma^2 + 1)\lambda^2 + 3S_\gamma^4\end{matrix}\right] \Big/ \lambda^4(\lambda^2 C_\gamma^2 - 1)^3 \tag{8}$$

No radial deformation (NH-NR): The engineering stress is calculated as: $\sigma = G(\lambda^2 - 1)(\lambda^2 + 3)/2\lambda^4$. The relation is rearranged to: $(2\sigma/G - 1)\lambda^4 - 2\lambda^2 + 3 = 0$; and solved for λ using the bi-quartic equation as:

$$\lambda = [-\sqrt{(4 - 6\sigma/G)} - 1)/(2\sigma/G - 1)]^{0.5} \tag{9}$$

The Gent (G) model with Constraints:

Uniaxial extension (G-UNI): The engineering stress is calculated as:

$$\sigma = GJ_m(\lambda^3 - 1)/[\lambda(-\lambda^3 + \lambda J_m + 3\lambda - 2)] \tag{10}$$

This equation is numerically solved for λ (up to the range of $\lambda = 2$) as:

$$\lambda = -0.015\left(\frac{\sigma}{G}\right)^3 + 0.17\left(\frac{\sigma}{G}\right)^2 + 0.31\left(\frac{\sigma}{G}\right) + 1 \tag{11}$$

Inextensible fiber (G-INF): The engineering stress as a function of elongation and the braiding angle is expressed in Appendix 1.

No radial deformation (G-NR): The engineering stress is calculated as:

$$\sigma = GJ_m\left[(\lambda^4 - 1)/(J_m\lambda^4 - \lambda^6 + 2\lambda^4 - \lambda^2) + (1/2\lambda^2)(\ln\left(1 - \left(\lambda - \frac{1}{\lambda}\right)^2/J_m\right))\right] \tag{12}$$

This equation is numerically solved for λ (up to the range of $\lambda = 1.8$) as:

$$\lambda = 0.9549e^{0.5157(\frac{\sigma}{G})} + (7.16 \times 10^{-11})e^{32.98(\frac{\sigma}{G})} + (4.5 \times 10^{-2}) \tag{13}$$

B.2- Continuum Manipulator Model

Considering the entire body, the manipulator model is discretized into serially-connected infinitesimal segments to generate a small-deflection beam [86] in each segment. We denote the initial segment length as ξ_0. Starting from the distal tip to the proximal base, a Cosserat rod model can be employed to formulate the Newtonian force equilibrium on each infinitesimal element, where each of these local deflections contribute to the final configuration as a whole by integrating over volume for the quasi-static case, eventually leading to an overall VC behavior.

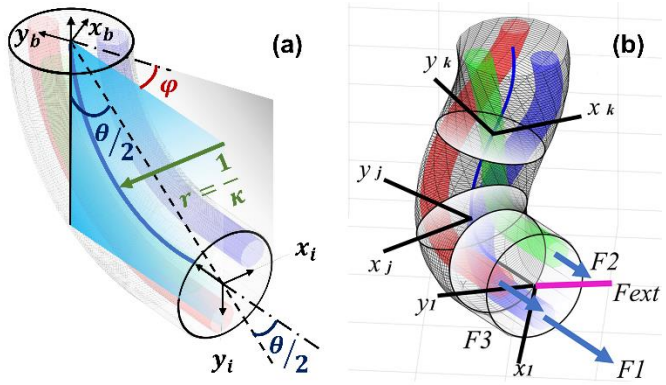

Fig.2: (a) Three arc parameters: Total arc length, bending angle θ (or curvature κ), and out of plane angle φ. (b) 3D simulation with actuation and external load causing bend, shear, torsion and extension – discretization and transfer of frames is selectively displayed.

The incremental elongated length of the backbone in each section is calculated as the summation of all chambers' new lengths divided by three:

$$\delta s_b = \frac{\sum_{j=1}^{3}[\xi_{0,i}(1+\lambda_i)]}{3} \tag{14}$$

The local bending moment vector due to internal actuation at each section w.r.t the backbone of the manipulator is calculated by the cross product of the distance to the center: $\boldsymbol{M}_i = \boldsymbol{d} \times \sum \boldsymbol{F}_i$ where $\boldsymbol{F}_i$ is the force due to intrinsic actuation. The local bending moment vector due to external load at each section is calculated by:

$$\boldsymbol{M}_e = \delta s_b [0,0,-1]^T \times \boldsymbol{F}_e \tag{15}$$

where F_e is the total boundary load at each incremental section, being transferred from the previous section. Therefore, the total local moment is calculated as: $\boldsymbol{M}_{tot} = \boldsymbol{M}_e + \boldsymbol{M}_i$. Projecting this moment vector onto its local x and y components delivers curvature/torsion in the local frame, $\boldsymbol{k}_{\xi_i}$, along the backbone. The local strain caused by internal and external load is denoted as $\boldsymbol{\varepsilon}_{\xi_i}$. To derive the system differential mechanics, the curvilinear path can be considered as a concatenation of infinitesimal elements. The VC kinematics is expressed with the following two differential equations for the Cartesian position vector $\boldsymbol{\rho}(s)$ and rotation matrix $\boldsymbol{R}(s)$ of each point along the backbone w.r.t $\boldsymbol{\varepsilon}$ and $\boldsymbol{k}$ (The dependency of the terms on s are omitted hereafter for brevity). Hence:

$$\begin{aligned} \boldsymbol{\rho}_{,s} &= \boldsymbol{R}(\boldsymbol{\varepsilon} + [0,0,1]^T)ds \\ \boldsymbol{R}_{,s} &= \boldsymbol{R}[\boldsymbol{k}]_\times \end{aligned} \tag{16}$$

Where $y_{,x} = \partial y/\partial x$ and $[\boldsymbol{x}]_\times = \boldsymbol{X}$ is an operator creating a skew-symmetric matrix $\boldsymbol{X}$ from a vector $\boldsymbol{x}$. The set of differential equations in (16) are to be numerically integrated over the spatial domain. For such equations, optimization-based methods, approximate continuous solutions, and FEM are conventionally employed. Alternatively, by considering a fixed number of elements n_s with length $\delta s = s_{total}/n_s$, we can rewrite Eq. (16) in the discrete form as:

$$\begin{aligned} \boldsymbol{\rho}_{(i+1)} &= \boldsymbol{\rho}_i + \boldsymbol{R}_i(\boldsymbol{\varepsilon}_i + [0,0,1]^T)\delta s \\ \boldsymbol{R}_{(i+1)} &= \boldsymbol{R}_i + \boldsymbol{R}_i[\boldsymbol{k}_i]_\times \delta s \end{aligned} \tag{17}$$

The transformation matrix from one segment to the other is composed as:

$$\boldsymbol{T}_{i+1} = \begin{bmatrix} \boldsymbol{R}_{i+1} & \boldsymbol{\rho}_{i+1} \\ \boldsymbol{0}^T & 1 \end{bmatrix} \tag{18}$$

were $\boldsymbol{0}$ denotes the 3×1 zero vector.

Finally, the overall transformation matrix from the tip to the base is formed as a multiplication of all transformations:

$$\boldsymbol{T}_n^0 = \left(\prod_{n-1}^{0} \boldsymbol{T}_{tot}\right) \boldsymbol{T}_n^{n-1} \tag{19}$$

where Π is the post-multiplication operator. The inverse of the final product, $\boldsymbol{T}_n^{0\,-1}$, multiplied by the previously stored $3 \times n$ matrix of coordinates would transform all coordinates to the base-frame representation; i.e., the first frame becomes the base, and the last frame becomes the distal tip. An alternative method for forming the transformation matrices in this discretized setup is provided in Appendix 2.

C. SETUP

We demonstrate the effectiveness of the above modeling strategy via experiments. The schematic interconnection of the setup's main components is depicted in Fig.3:

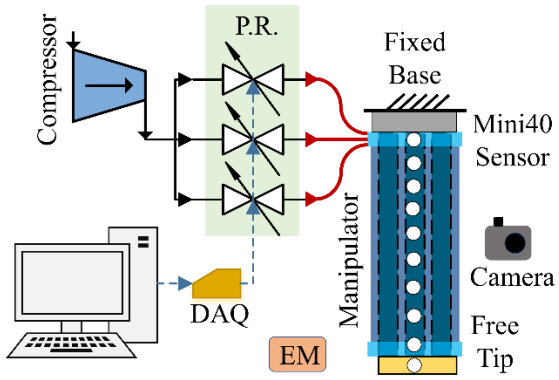

Fig.3: The setup consists of an air compressor, 3 pressure regulators (P.R.), data acquisition board (DAQ), camera, visual markers, EM tracking system, and the manipulator; interconnected with necessary tubing and wiring.

Pressurized air from the compressor (BAMBI MD Range Model 150/500) is supplied to three individual pressure regulators (SMC ITV0030-3BS-Q); with their outlet each separately connected to one of the dual chambers in the manipulator for adjusting the pressure to achieve manipulator operation, according to the command received from the computer (64-bit Windows 10; Intel Core i7 CPU @ 3.4GHz; 64GB RAM) through a DAQ board (NI USB-6411). One Aurora sensor (NDI) is placed at the fixed base, and one at the tip for tracking the spatial tip position. Monitoring the overall pose is made possible by marking additional 8 points on the body which are recorded via two cameras (Canon EOS D60) facing the manipulator from two directions perpendicular to each other, and the progression of the marked points are monitored via the open source program Tracker 4.96 (www.opensourcephysics.org). The diameter of the marked points averaged at 1.5mm and were tracked with ~0.5mm tolerance. An ATI Mini40 force sensor reads the resultant forces at the fixed base (Fig.1(c)). The data acquisition software is coded in C++.

Initially we consider the deformation, both in the absence and in the presence of external loads. We characterize E considering the different modelling assumptions discussed earlier. Thereafter, the manipulator is used for contact force estimation based on the obtained results from the previous stage. For tip force sensing, external force is applied at an ATI Nano17 force sensor affixed to the tip (Fig.1(c)). For sensing forces applied on the body, the ATI Nano17 force sensor is mounted on an external indenter to exert force on the body of the manipulator (Figs.8, 9, 10, 11). In both cases, the manipulator is actuated in various configurations, and is deformed further by applying external force. We record the applied force in addition to the force measured at the base (via ATI Mini40 force sensor), while tracking the body deformation. Both force sensors are connected to the computer via NI PCIe-6320 I/O cards.

4. EXPERIMENTS AND ANALYSIS

In the following, we empirically discretized the length of 47mm of the robotic appendage to 100 sections for all simulations. It was observed that decreasing the number of sections to less than 30 tends to demonstrate significant deviations, while above 50 sections, the results are tangentially closer to 100 sections and deliver benign results.

A. Elasticity vs. Hyperelasticity in Braided Extensor Model

A closer look into the hyperelastic models reveals that as the thread angle is increased, the INF constraint demonstrates closer resemblance to the NR constraint in both the Neo-Hookean and Gent models; ultimately becoming the same in its limit at 90° (depicted in Fig.4 for the Gent model, setting E as a free parameter varying from 60 to 180kPa). Decreasing the thread angle less than ~70° in a single-braid configuration is usually not practiced, as it also undermines the primary role of reinforcement against radial expansion. As seen, 100% elongation ($\lambda = 2$) is achieved at a higher internal pressure when the thread angle is smaller, compared to thread angles closer to 90°.

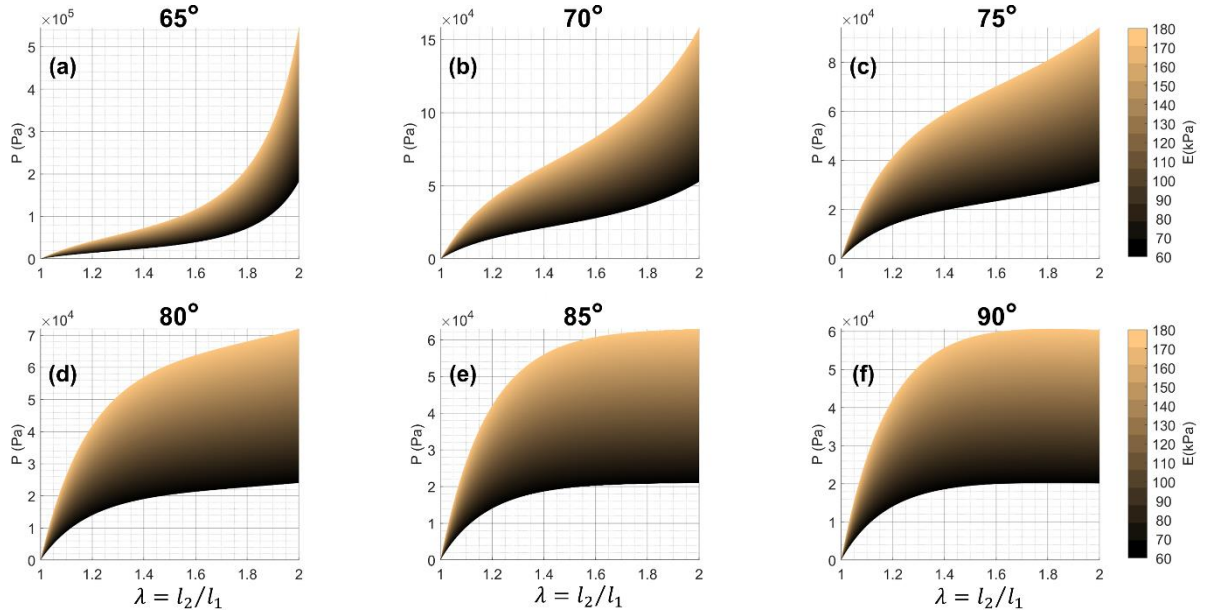

Fig.4: Gent model with INF constraint - Plotting internal pressure (Pa) vs. stretch, showing progression of the enveloped area (range of E = 60 to 180kPa) as the braiding angle is increased from 65° (a) to 90° (f). l_1 and l_2 are the initial and extended length, respectively. Thread angle is shown in Fig.1(a).

Inspection of the thread on the braided extensor in Fig.1(a) demonstrates dense braiding where the assumption of 90º for the thread angle is reasonable. Hence, we only examine UNI and NR constraints in both hyperelastic models. Moreover, the asymptotic progression in Fig.4(f) – thread angle 90° – shows that depending on the value of E, there exists a threshold internal pressure where the stretch (λ) perpetually increases; demonstrating how the model predicts continuous unwinding of the chain polymers when the radial deformation of the chamber is fully constrained. Hence using the hyperelastic models require caution when dealing with the NR constraint.

B. Elasticity vs. Hyperelasticity in Soft Manipulator Model

B.1- No External Load

The robotic appendage is actuated in 9 stages by giving an input voltage of 1v to each pressure regulator in turn, then increasing to 2v, and finally to 3v. The average pressure outlet corresponding to these voltages are tabulated in Table 1:

		Air Pressure Outlet (Pa × 10^5) from Each P.R.		
		P.R.1	**P.R.2**	**P.R.3**
Input Signal (v)	**1**	0.45	0.35	0.45
	2	0.92	0.87	0.91
	3	1.33	1.38	1.38

Table 1: Air pressure (Pa × 10^5) outlet from each pressure regulator (P.R.) resulting from the corresponding input signal (v).

The tip spatial coordinates and the bending angle are recorded. In order to determine how well the observed results are replicated by the model, the coefficient of determination (R^2) for the coordinates and the bending angle between the simulations and experiments are depicted in Fig.5, in which we set E as a free parameter varying from 60 to 180kPa.

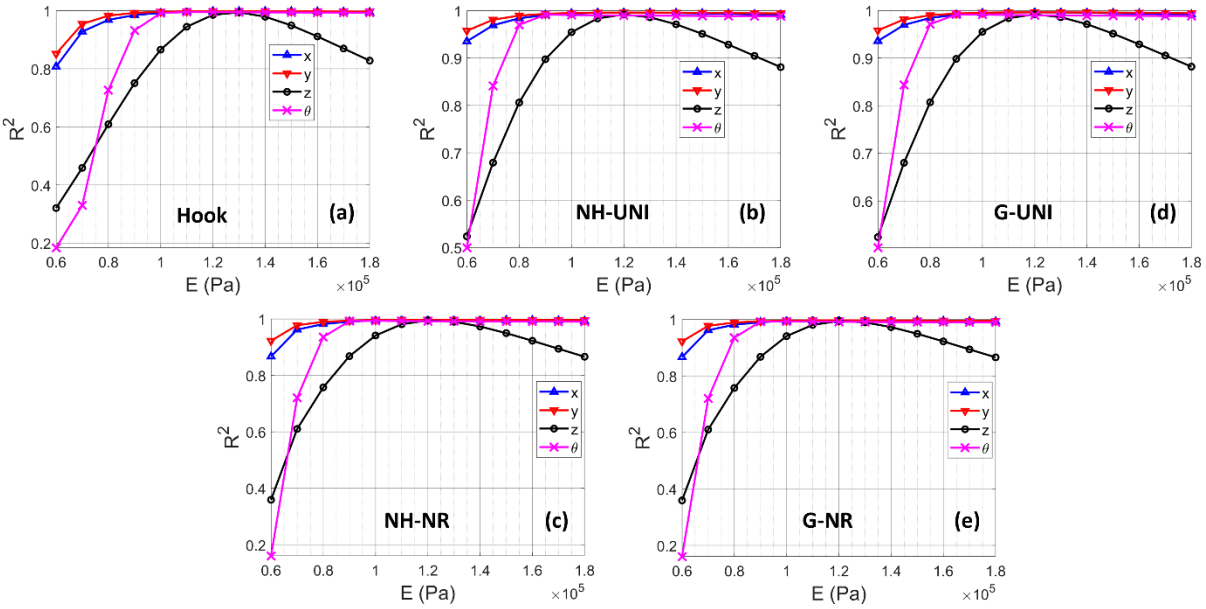

Fig.5: Experiments with no load, showing R^2 of tip coordinates between results from simulations and experiments across variations of E: (a) Hooke; (b) Neo Hookean-Uniaxial; (c) Neo Hookean-No Radial; (d) Gent-Uniaxial; (e) Gent-No Radial

In all cases, the highest values of R^2 (close to 1) correspond to an E in the range of 100 to 140 kPa. As it can be seen, the z coordinate displays sharper changes compared to the x, y coordinates especially at lower E values as opposed to higher values were the R^2 conformity degenerates at a slower rate, indicating higher sensitivity at lower values of Young's modulus. This could be attributed to the material constructing the robotic appendage body being more distributed along the z axis compared to x and y, which hold true even in a bent configuration on average.

Selecting E=130 kPa, we plot the test results of measured tip coordinates against the simulation using the Hooke relation. The absolute displacements are depicted in Fig.6(a) for each of the coordinates, where z coordinates start from -47mm which is the initial length. The x coordinate starts from -15mm which is the placement of the tip Aurora tracker. The absolute error for each coordinate as shown in subfigures (b)(c)(d). The coefficient of determination is calculated as ${R^2}_x$=0.998, ${R^2}_y$=0.998, ${R^2}_z$=0.994, ${R^2}_\theta$=0.995, which indicates very high conformity between experimental measurements and simulations results as the robotic appendage is actuated.

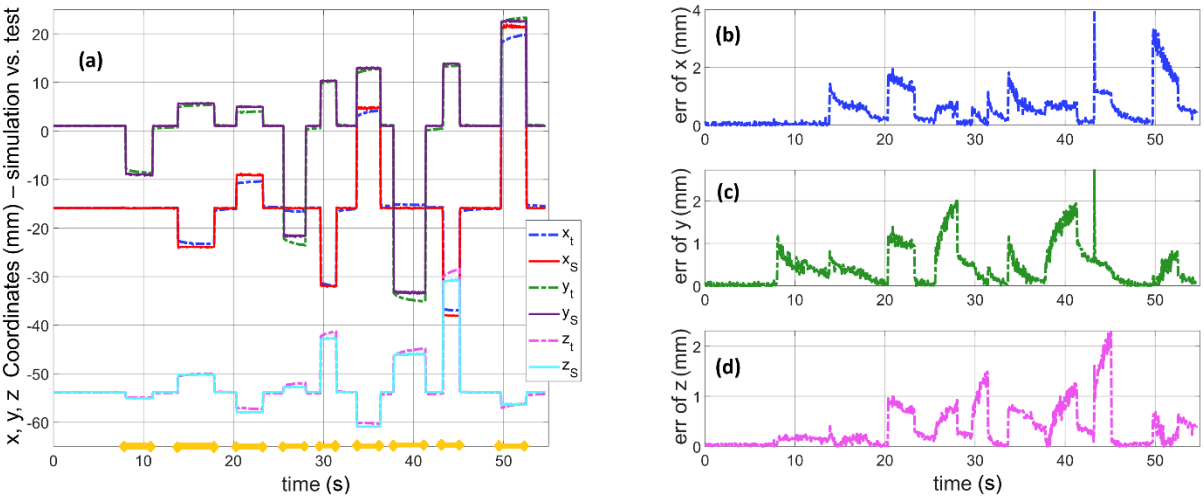

Fig.6: Left: Tip coordinates from test "t" compared against simulation "s". Right: the error in all three coordinates. Hooke model, setting E=130kPa. (No load) – 9 stages of actuation marked on the horizontal axis of (a).

With the manipulator discretized into 100 sections, the simulation operates at an execution rate of 170Hz in MATLB with no noticeable difference between the investigated methods.

The normalized tip error is calculated by measuring the error vector divided by the manipulator's initial length [31] [32]. To create a unique pressure metric, the three pressure values are treated as componenets of a pseudo-vector, and the norm is calculated. Fig.7 demonstrates how the tip normalized error changes with the norm of the pressure vector (from 0 to 1.5bar), across a variation of E from 60 to 180kPa.

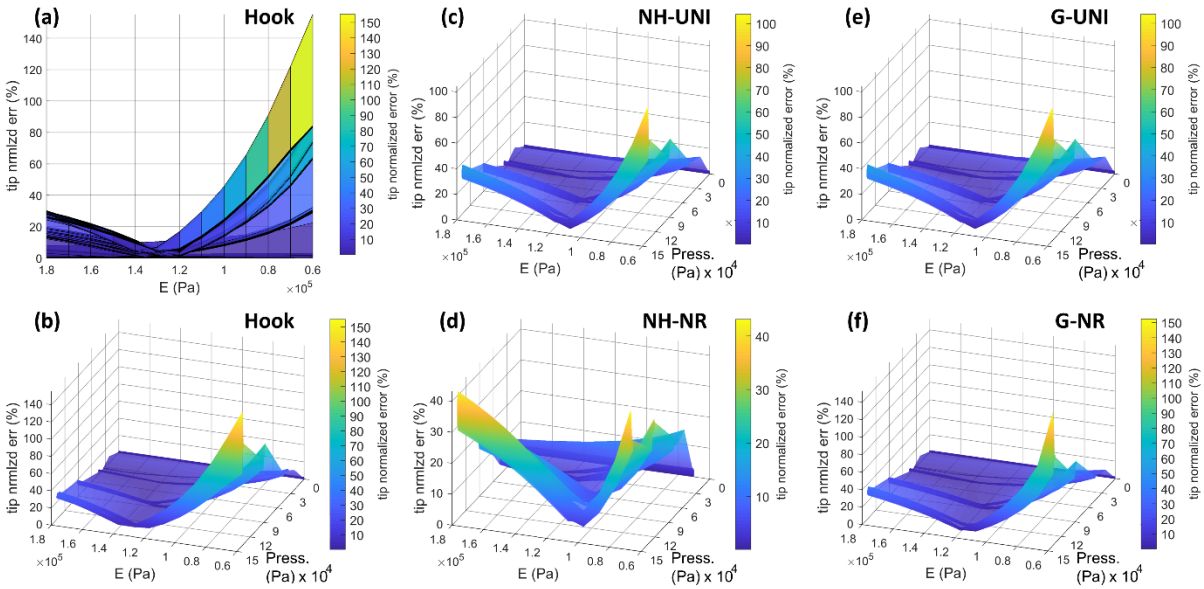

Fig.7: Normalized tip error vs. pressure across variation of E: (a) Hooke (y-z view); (b) Hooke; (c) Neo-Hookean Uniaxial; (d) Neo-Hookean No Radial; (e) Gent Uniaxial; (f) Gent No Radial. (No load)

As expected, the error at the tip increases at higher pressures; however, where the value of E corresponds to the lowest error (in the range of 100 to 140kPa), a more uniform distribution of error with the increase of pressure is witnessed, forming the trough in the 3D surfaces. Taking the Hookean model as an example, a clearer demonstration is shown in Fig.7(a) - a 2D view of the graph in Fig.7(b), at E ~130kPa. These graphs also reaffirm that change of E at its lower levels affects the error more severely compared to at its higher values (above ~130kPa).

B.2- External Load

Tests with external load were performed with load applied in various configurations; at the tip (Fig.1), and on the body at the first, second, third and fourth quarter of its length (Fig's 8,9,10,11). The ATI Nano17 recorded the applied force and the ATI Mini40 recorded the forces measured at the base. The overall pose was observed by tracking 10 points on the body. The range of external load varied in different configurations from 0.46N up to 1.79N based on the contact point and the deformation, with a more detailed report in the following section.

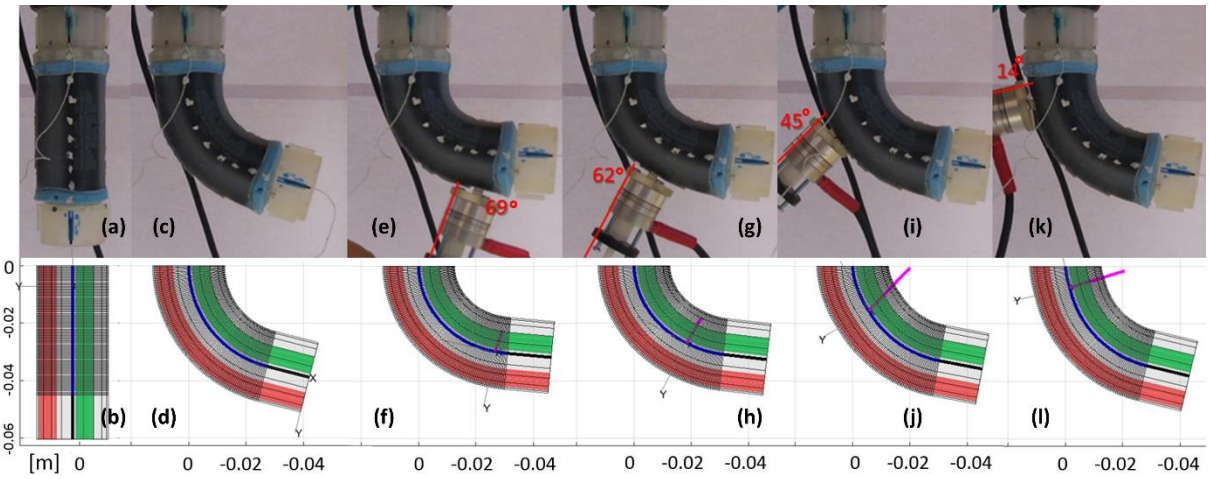

Fig.8: Applying an external load along the body in bent configuration on the first, second, third and fourth quarters with the Nano17 affixed to an external indenter, along with simulation results. Images (a) and (b) show the initial configuration.

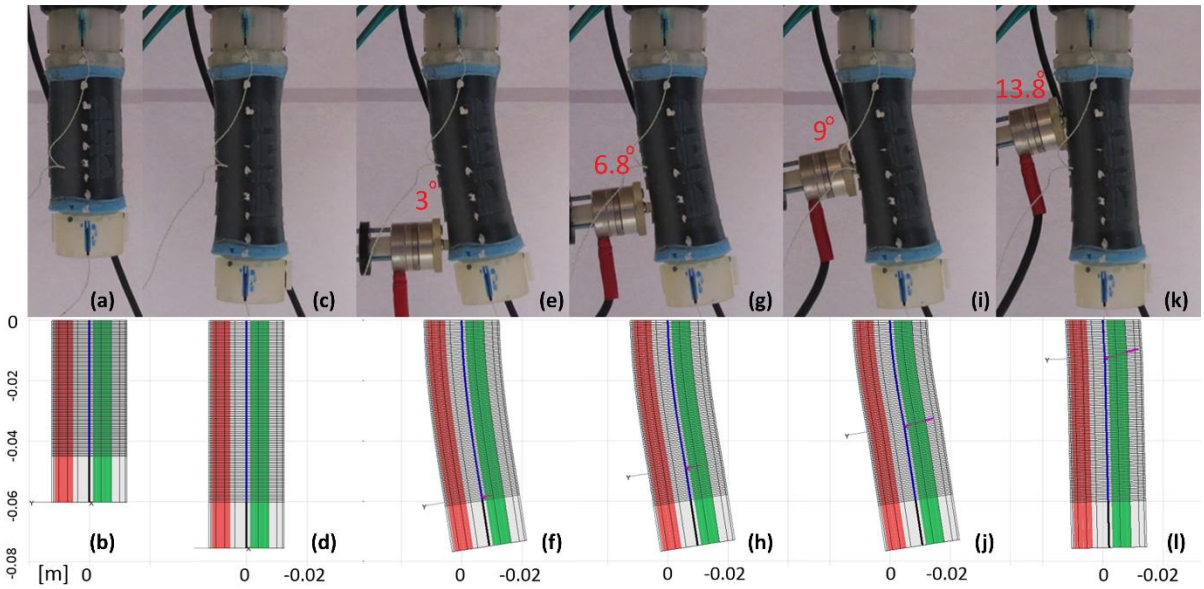

Fig.9: Applying an external load along the body on the first, second, third and fourth quarters, in a straight elongated configuration, along simulation results. Images (a) and (b) show the initial configuration.

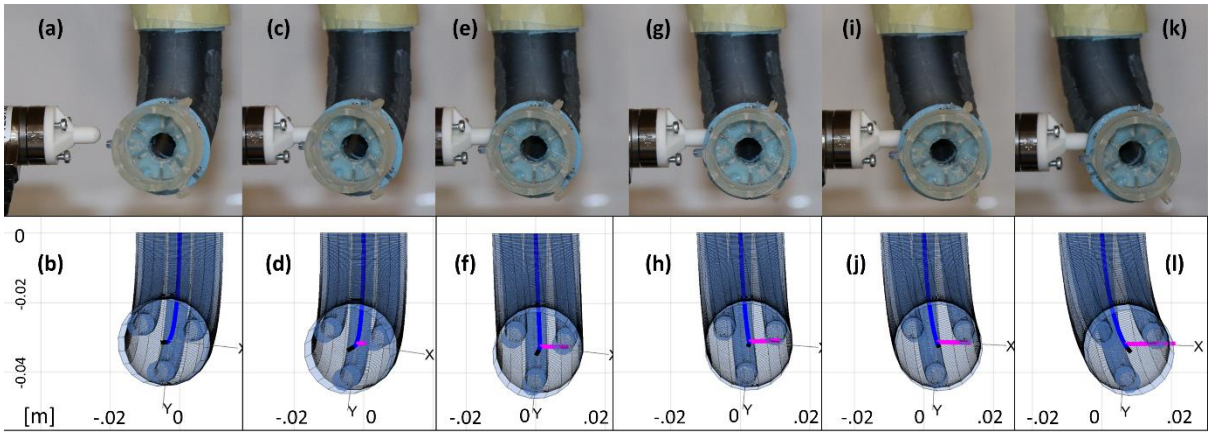

Fig.10: Applying an external load along the body on the first quarter of soft appendage length from the tip, in a bent configuration, along simulation results. Images (a) and (b) show the initial configuration.

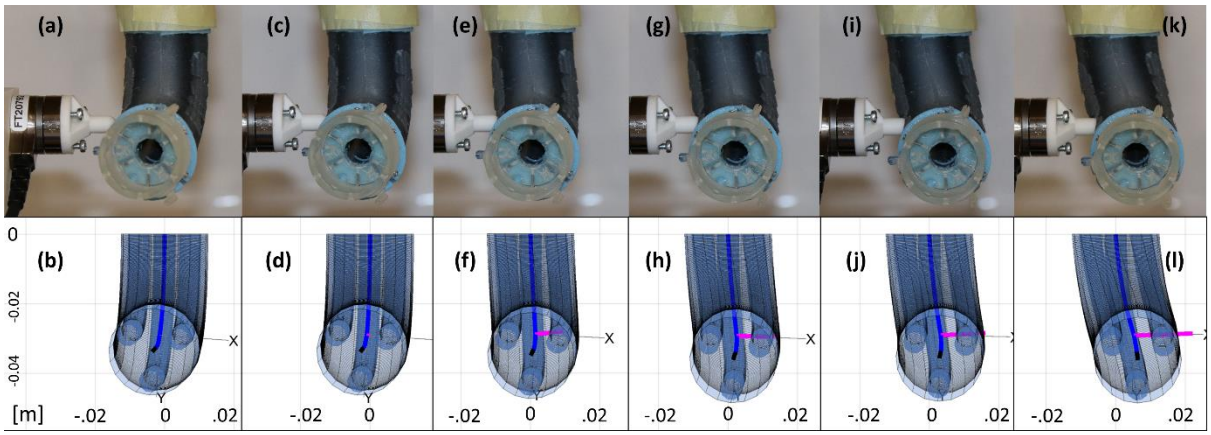

Fig.11: Applying an external load along the body on the second quarter of soft appendage length from the tip, in a bent configuration, along simulation results. Images (a) and (b) show the initial configuration.

The robotic appendage was initially activated via pressurization and the overall pose was recorded. Applying an external force caused additional deformation. In all cases of the elastic and hyperelastic assumptions detailed earlier, we calculated the normalized error of all 10 points on the body which is averaged at each location over all tests, and depicted in Fig.12 on the vertical axis (0 to 30%), across the variation of E from 60 to 180kPa, and the initial distance from tip (0 to 60mm):

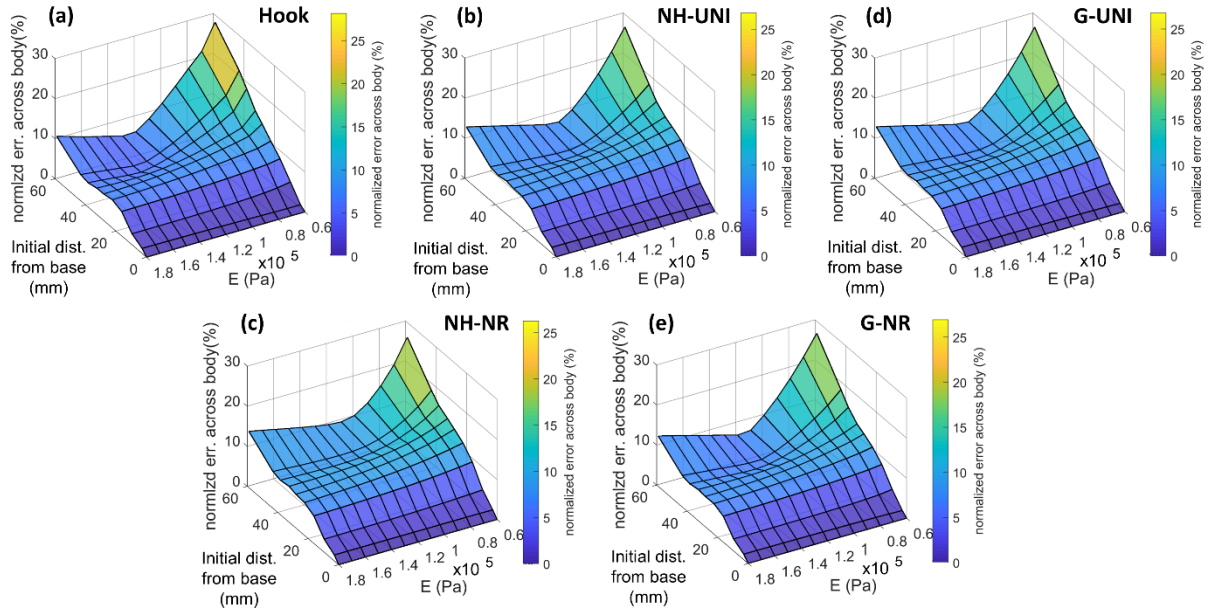

Fig.12: Experiments with external load on the robotic appendage. Variation of normalized error of 10 points along the body (from tip to base) along different E's. (a) Hooke; (b) Neo-Hookean Uniaxial; (c) Neo-Hookean No Radial; (d) Gent Uniaxial; (e) Gent No Radial.

At any chosen value for E, the error increases from base to tip (which is expected), in all graphs. The error variations at the tip across E lead to a convex profile. Closer inspection reveals that the curve minimum not only indicates the E value yielding the least amount of error at the tip (in the range of 100 to 140kPa for the different cases), but also across the length of the manipulator, forming a trough in the corresponding 3D surface. Taking the Hooke approach as an example, this could be observed around an E of almost 130kPa, shown in Fig.12(a). As seen before, variation of E at lower values (in the range of 60 to ~100kPa) affects the error more than at the higher E values, demonstrating higher sensitivity to lower E's. Fig.13(a, c, e, g, i) summarizes the simulation results for all categories discussed earlier. The normalized error is plotted for the tip (considering three cases: no external load, external load at tip, and external load on body) on the vertical axis; and for all tracked points on the body (with force at the tip and force on the body). The standard deviation of the normalized error of all recorded points are shown in Fig.13(b, d, f, h, j) for tip load and body load cases, which demonstrate lower values in the range of 100 to 140kPa for E, depending on the model. As seen, loading applied to the body tends to result in a sharper sensitivity to the variation of E. The results are summarized in Table 2. In all columns, the Young's modulus which corresponded to the least error or least standard deviation, respectively, is presented.

		External Load at Tip						**External Load on the Body**						**No Ext. Load**	
		§	*E*	†	*E*	‡	*E*	§	*E*	†	*E*	‡	*E*	‡	*E*
Hooke		5.3%	*140*	2.2	*130*	6.3%	*130*	2.7%	*130*	1.0	*130*	4.3%	*130*	1.8%	*130*
NH	UNI	6.6%	*120*	2.6	*120*	7.8%	*110*	4.1%	*110*	1.5	*110*	5.6%	*110*	2.6%	*110*
	NR	7.4%	*130*	2.9	*120*	9.8%	*110*	5.7%	*100*	2.6	*95*	8.9%	*95*	3.4%	*110*
G	UNI	6.6%	*120*	2.6	*120*	7.8%	*110*	4.1%	*110*	1.5	*110*	5.7%	*110*	2.6%	*110*
	NR	6.2%	*120*	2.4	*120*	7.1%	*120*	3.9%	*110*	1.4	*110*	4.6%	*110*	2.1%	*120*

Table 2: (§) average normalized error across body; (†) STD of normalized error across body; (‡) average normalized tip error.

In general, it can be seen that the Hooke formulation provides results with the least error compared to the Neo-Hookean and the Gent hyperelastic models.

Although to the best of our knowledge, the detailed analysis on positional error was not witnessed in similar research works, yet comparing with some other approaches, our model shows to be the most accurate solution for a two-segment construction of this same manipulator, compared to a polynomial of order three where an average of 6% mean error is observed for the static model in 2D, and 8% in 3D motion using both the Ritz and Ritz-Galerkin method [41]. Other methods yield errors as: 31% in CC; 28% in principle of virtual work using CC kinematics; 6-12% in the Cosserat rod model; 11% in approximate solutions similar to [39] in the static case; and 22% in the lumped system model in the dynamic case [42].

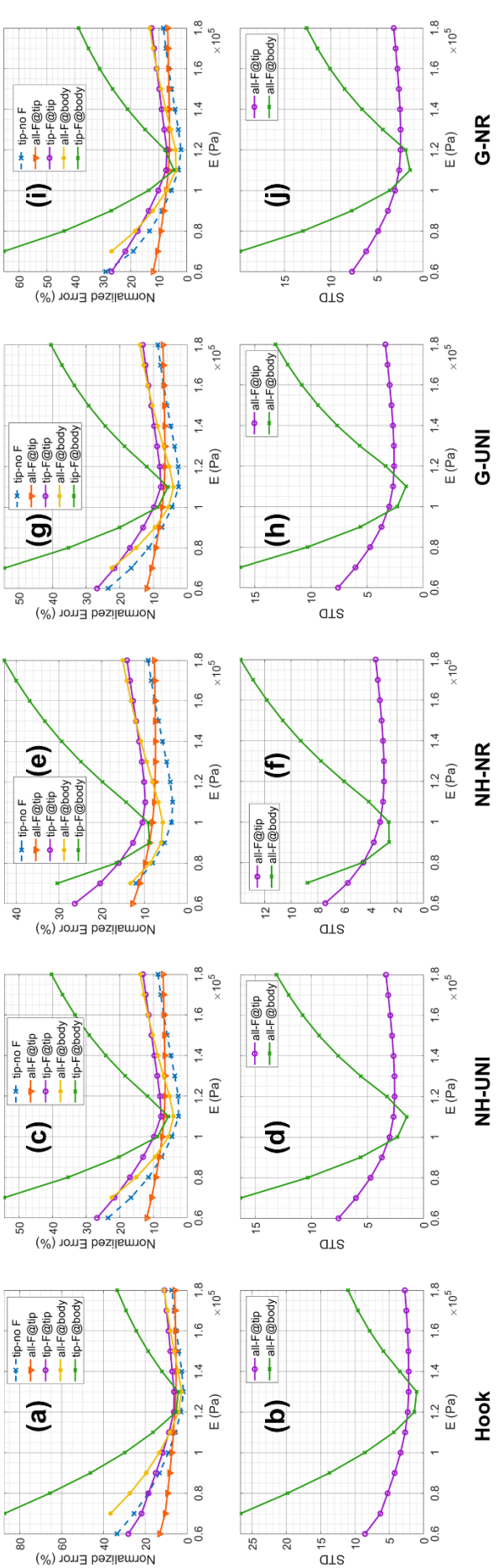

Fig.13: Normalized error of tip and entire body for (a) Hooke, (c) Neo-Hookean UNI, (e) Neo-Hookean NR, (g) Gent UNI, (i) Gent NR; Standard Deviation (STD) of tip and entire body for (b) Hooke, (d) Neo-Hookean UNI, (f) Neo-Hookean NR, (h) Gent UNI, (j) Gent NR.

C. Force Estimation

Based on the results obtained, we select the Hooke formulation for contact force estimation. Four general cases were investigated as follows. In all cases, the simulation runs at an execution rate of about 170Hz in MATLB with the robotic appendage being discretized into 100 sections.

C.1- External load applied at the tip

For this case, the robotic appendage was actuated via the 3 pressure regulators (P.R.) in turn according to the 9 separate schemes in Fig.14-table(a), and force was applied at the Nano17 force sensor affixed at the tip. The average of the maximum applied force across the 9 schemes is 1.35N, and the total average of the applied force is 0.94N. The mean absolute error in each actuation scheme, plotted in Fig.14 (b), is calculated as:

$$MAE = \frac{\sum_{i=1}^{n} |e_i|}{n}$$

where e_i is the error between sensor reading and model estimation at each sensor reading cycle i, during all n cycles. The normalized error in each scheme is calculated by two methods: w.r.t the maximum force, according to: (MAE/F_{max}); and w.r.t the average amount of force, according to: (MAE/F_{ave}); displayed in Fig.14(c). The coefficient of determination, R^2, is depicted in Fig.14(d).

(a)

Actuation Scheme No.	Input signal (v) P.R.1	P.R.2	P.R.3
1	1	0	0
2	1	1	0
3	1	1	1
4	2	0	0
5	2	2	0
6	2	2	2
7	3	1	0
8	3	3	0
9	3	3	3

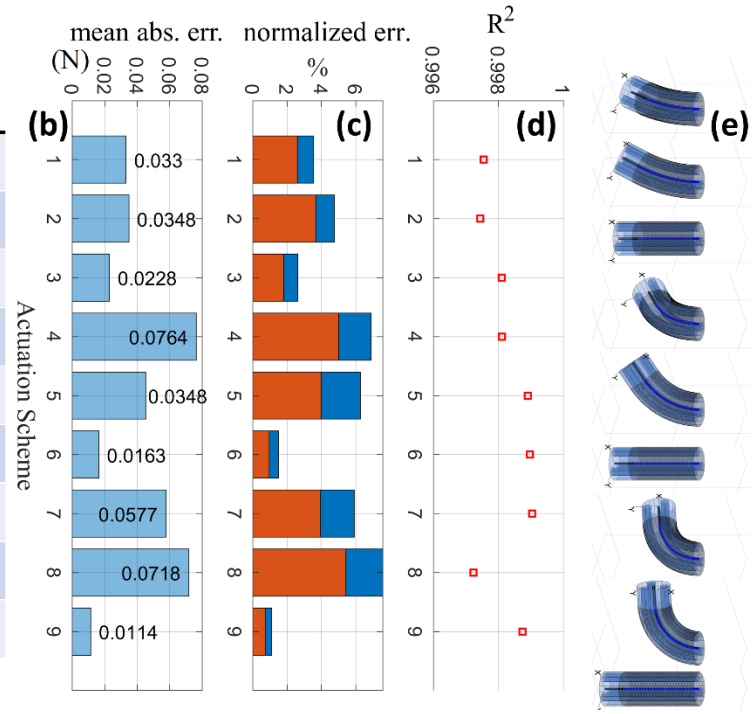

Fig.14: Load at the tip: (a) The three P.R.'s are activated according to the tabulated nine schemes. (b) Mean absolute error. (c) MAE/F_{max} (red), and MAE/F_{ave} (blue). (d) R^2 of model w.r.t test. (e) Simulated activation schemes.

C.2- External load applied to the body

For this case, the pressure regulators were actuated to generate maximum bend, according to table (a) in Fig.15. Considering four quarters along the robotic appendage's length, an external load was applied on the body within each quarter of the length in turn, from the distal end towards the base (Fig.15(e)); constituting four force application schemes. The average of the maximum applied force across the 4 schemes is 1.15N, and the total average of the applied force is 0.85N. Similar to the previous case, the mean absolute error, normalized errors, and R^2 are calculated, and displayed in Fig.15.

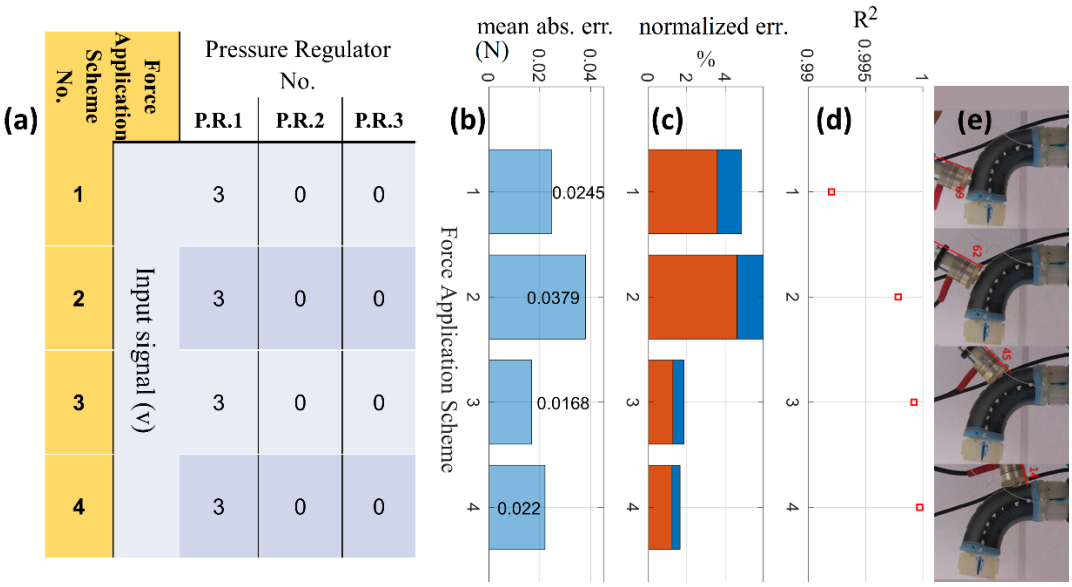

Fig.15: Load on the body: (a) In all four schemes of applying load, the three P.R.'s are activated according to the table for maximum bending. (b) Mean absolute error. (c) MAE/F_{max} (red), and MAE/F_{ave} (blue). (d) R^2 of model w.r.t test. (e) Activation and external load

C.3- Stepwise Lateral External load

To demonstrate the effectiveness of the model prediction w.r.t the out-of-plane applied load, the robotic appendage was actuated to maximum bending and an external load was laterally applied via an indenter, at the tip and on the body (in turn within the 1st and 2nd quarters of the length from the tip). The magnitude of the load was increased during four steps. The average of the maximum applied force across the 3 schemes is 1.0N, and the total average of the applied force is 0.51N. The mean absolute error, normalized errors, and R^2 are calculated, and displayed in Fig.16.

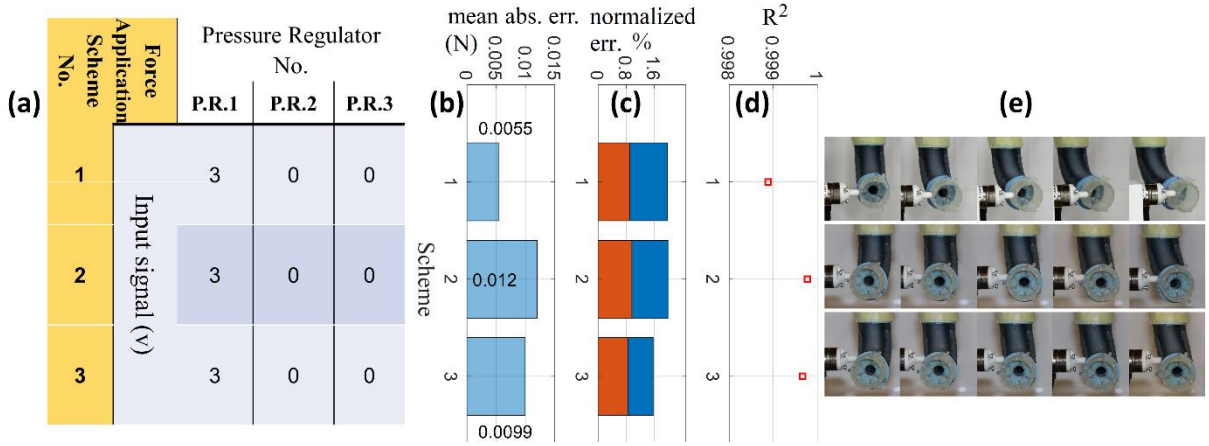

Fig.16: Stepwise load: (a) In all three schemes of applying load, the three P.R.'s are activated according to the table for maximum bending. (b) Mean absolute error. (c) MAE/F_{max} (red), and MAE/F_{ave} (blue). (d) R^2 of model w.r.t test. (e) External load applied in steps.

The results of all three cases (C1, C2, C3) are summarized in Table 3.

Case	MAE			(MAE/Fmax)			(MAE/F$ave.$)			R^2
	max.	ave.	min.	max.	ave.	min.	max.	ave.	min.	ave.
C1	0.076	0.041	0.011	5.43%	3.13%	0.73%	7.58%	4.47%	1.1%	0.998
C2	0.038	0.025	0.0168	4.61%	2.67%	1.23%	5.98%	3.58%	1.85%	0.997
C3	0.012	0.009	0.005	0.96%	0.91%	0.85%	1.98%	1.84%	1.57%	0.999

Table 3: Summary of MAE, normalized MAE's, and R^2 for the three cases of C1, C2, C3.

Considering the three mentioned cases, the maximum normalized error w.r.t the averaged applied force is less than 8%. In all cases we witness very high values of above 0.99 for R^2, demonstrating high accuracy of the model predicting the external load.

C.4- Cyclic External load

For investigating the effect of cyclic load increase/decrease, the robotic appendage was actuated to maximum bending (~90°), and a cyclic force was applied at the tip where the Nano17 was affixed while increasing and decreasing the loading in 5 cycles. The force components and the magnitude of force of the test and the simulation are plotted against each other in Fig.17. The average of the maximum applied force across is 0.46N, and the total average of the applied force is 0.17N across time. Results show a mean absolute error of 0.015N for the force magnitude, and an R^2 of 0.99. The absolute errors are depicted in Fig.18.

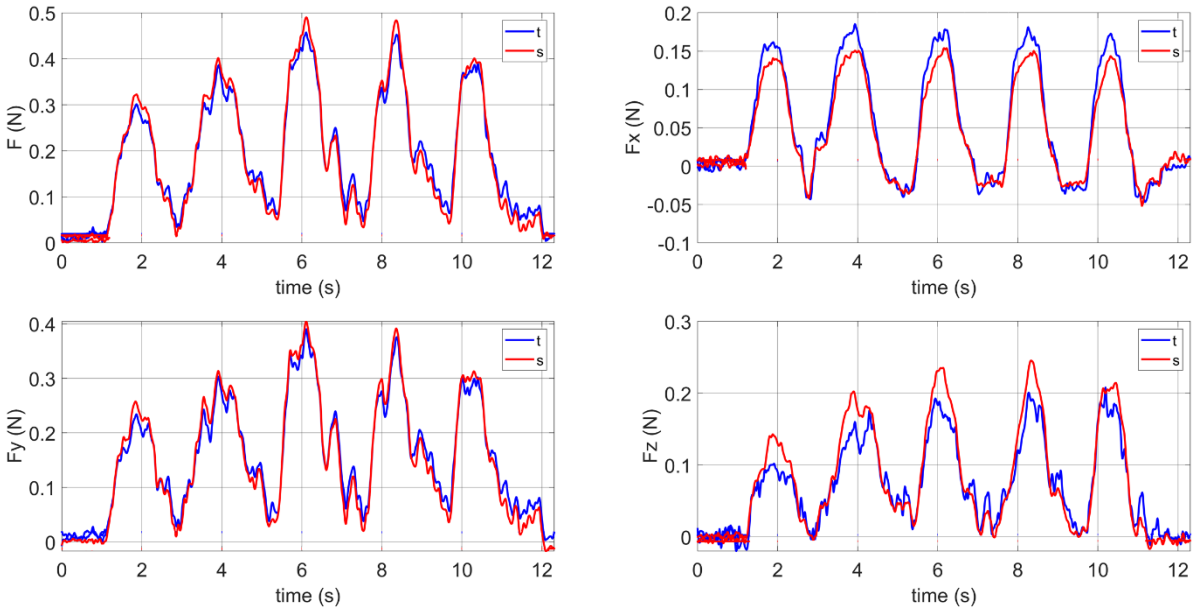

Fig.17: Comparison between force sensor readings "t", and model estimation "s": (a) total magnitude of forces, (b) Fx, (c) Fy, (d) Fz.

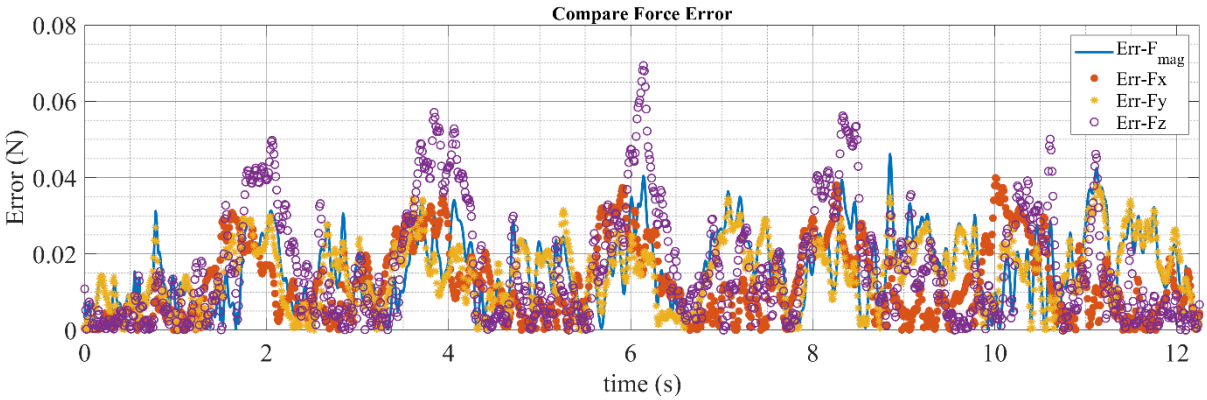

Fig.18: Absolute error between sensor reading and simulation for force magnitude, Fx, Fy, and Fz.

5. REPEATABILITY

Repeatability was investigated in three scenarios, by pressurizing the manipulator to its practical extreme configurations (bending and stretch) and applying external force at the tip to generate more deformation and internal stress compared to applying the force elsewhere; across three trials. The average of the force magnitude at the base along with the Standard Deviation in each case is reported in Table 4. Due to limited strain, the soft appendage demonstrated good repeatability.

Average Force Magnitude at Base (N)	2.50		0.44		0.53	
STD of Force	0.025		0.034		0.011	

Table 4: Three scenarios: A) Maximum bending, external load applied at the tip in line with the soft appendage's backbone; B) Maximum bending, external load at the tip laterally; C) Maximum stretch, external load at the tip laterally.

6. CONCLUSIONS

In this paper, we presented mathematically straightforward yet comprehensive approach for modelling and real-time simulation of a silicon-based pneumatic soft continuum robotic appendage comprising braided extensors in quasi-static movements. The proposed model takes into account the effects of internal and external forces with regards to bending, shear, torsion, and extension, and transfers these effects along the entire backbone leading to a 3D kinematic deformation. We comparatively investigated three approaches (Hooke, Neo-Hookean, and Gent) to determine the best conformity between the model and experiments (performed with the STIFF-FLOP manipulator). The latter two hyperelastic models were each separately considered with two different constraints: uni-axial deformation, and no-radial deformation. In each case, we derived the principal stretch as a function of stress for braided extensors.

Experiments were performed without load and with load; applied at the tip and along the body on multiple points. In all cases, we studied the response by setting the Young's modulus (E) as a free parameter ranging from 60 to 180kPa, and we investigated the value with most conformity. It was seen that for this type of robotic appendage which experiences only limited strains, the Hookean model provided a marginally better estimate for position/deformation and force analysis, with a higher predicted value for E compared to the two hyperelastic models investigated. We also observed that variations of E at lower actuation pressure have a significantly less negative effect on the model prediction as opposed to higher pressures. Furthermore, the prediction from the model does not vary

linearly w.r.t to E, as lower values for E result in sharper changes in error compared to higher values. Selecting 100 sections for the robotic appendage, the simulation is able to run at 170 Hz in MATLB on the computer with the specifications mentioned in section 3 part C; and most likely to improve by implementing the modelling with a lower level language. This execution rate suffices for real-time applications, and as a result of the proposed approach, enables access to internal forces across (almost) the entire backbone, which is as an important feature for monitoring the health of the system in addition to facilitating embodied force perception.

We conclude that the Hookean assumption is valid for a silicone-based robotic appendages at small strains (about 50% in extension/compression [83]). This result indicates that research works with similar robotic platforms may not necessarily require hyperelastic analysis. The exact range of this validity w.r.t. dimensional and/or actuation limits is yet to be determined, and beyond the scope of this study. Further examination on this is included in Appendix 3.

The proposed model's versatility in estimating external forces applied anywhere on the body and reporting the force values, empowers real-time force sensing and perception in these class of manipulators leading to wider range of practical applications for safe human robot interaction. This transformation of pose/force information from one section to the next in the discretized setting can be implemented for any similar platform consisting of multiple segments. In other words, the existing single segment can be treated as multiple virtual segments without loss of accuracy, with potential extension and application of the approach to multi-segment robots for future studies. The limitation depends on maintaining the assumptions in section 3-A. Another interesting area for additional investigation would be exploring the ability to predict the location of applied force.

Structural imperfections resulting from hand construction (especially in the braided extensors) causes some discrepancies in behavior which are not reflected in the model; e.g. the extension of the fluidic chambers when subject to pressurization was observed to not be exactly homogenous. In this regard, introducing compensating terms can improve the performance however at the cost of losing generality, and were not considered here. Finally, although the current implementation of the model could cope with multiple and/or distributed loads, however it would require an iterative procedure with an impact on computational cost, with its feasibility for force estimation to be pursued in future work.

7. ACKNOWLEDGMENTS

This research has received funding from the EU FP7 project STIFF-FLOP grant No. 287728 and the UK EPSRC project MOTION grant No. EP/N03211X/2 and Leverhulme Trust Project RPG-2016-345.

8. AUTHOR DISCLOSURE STATEMENT

No competing financial interests exist.

9. REFERENCES

1. Cianchetti, M. *et al.* Soft Robotics Technologies to Address Shortcomings in Today's Minimally Invasive Surgery: The STIFF-FLOP Approach. *Soft Robot.* **1,** 122–131 (2014).

2. DeGreef, A., Lambert, P. & Delchambre, A. Towards flexible medical instruments: Review of flexible fluidic actuators. *Precis. Eng.* **33,** 311–321 (2009).

3. DeFalco, I., Cianchetti, M. & Menciassi, A. A soft multi-module manipulator with variable stiffness for minimally invasive surgery. *Bioinspiration and Biomimetics* **12,** (2017).

4. Katzschmann, R. K., Marchese, A. D. & Rus, D. Autonomous Object Manipulation Using a Soft Planar Grasping Manipulator. *Soft Robot.* **2,** 155–164 (2015).

5. Wang, L. & Iida, F. Deformation in Soft-Matter Robotics: A Categorization and Quantitative Characterization. *IEEE Robot. Autom. Mag.* **22,** 125–139 (2015).

6. Renda, F. *et al.* Dynamic Model of a Multibending Soft Robot Arm Driven by Cables Dynamic Model of a Multibending Soft Robot Arm Driven by Cables. *IEEE Trans. Robot.* **30,** 1109–1122 (2014).

7. Wehner, M. *et al.* An integrated design and fabrication strategy for entirely soft, autonomous robots. *Nat. Lett.* **536,** 451–455 (2016).

8. Rus, D. & Tolley, M. T. Design, fabrication and control of soft robots. *Nature* **521,** 467–475 (2015).

9. Cianchetti, M., Calisti, M., Margheri, L., Kuba, M. & Laschi, C. Bioinspired locomotion and grasping in water: The soft eight-arm OCTOPUS robot. *Bioinspiration and Biomimetics* **10,** (2015).

10. Eder, M., Hisch, F. & Hauser, H. Morphological computation-based control of a modular, pneumatically driven, soft robotic arm. *Adv. Robot.* **1864,** 1–11 (2017).

11. Wang, Z. *et al.* Interaction Forces of Soft Fiber Reinforced Bending Actuators. *IEEE/ASME Trans. Mechatronics* **22,** 717–727 (2017).

12. Thuruthel, T. G., Ansari, Y., Falotico, E. & Laschi, C. Control Strategies for Soft Robotic Manipulators: A Survey. *Soft Robot.* **5,** 149–163 (2018).

13. Camarillo, D. B., Milne, C. F., Carlson, C. R., Zinn, M. R. & Salisbury, J. K. Mechanics modeling of tendon driven continuum manipulators. *IEEE Trans. Robot.* **24,** 1262–1273 (2008).

14. Giorelli, M. *et al.* Neural Network and Jacobian Method for Solving the Inverse Statics of a Cable-Driven Soft Arm with Nonconstant Curvature. *IEEE Trans. Robot.* **31,** 823–834 (2015).

15. Tatlicioglu, A. E., Walker, I. D. & Dawson, D. M. Dynamic Modelling for Planar Extensible Continuum Robot Manipulators. in *IEEE International Conference on Robotics and Automation (ICRA)* 1357–1362 (2007). doi:10.1109/ROBOT.2007.363173

16. Polygerinos, P. *et al.* Modeling of Soft Fiber-Reinforced Bending Actuators. *IEEE Trans. Robot.* **31,** 778–789 (2015).

17. Camarillo, D. B., Carlson, C. R. & Salisbury, J. K. Configuration tracking for continuum manipulators with coupled tendon drive. *IEEE Trans. Robot.* **25,** 798–808 (2009).

18. Jones, B. A., Gray, R. L. & Turlapati, K. Three dimensional statics for continuum robotics. in *IEEE/RSJ International Conference on Intelligent Robots and Systems (IROS)* 2659–2664 (2009). doi:10.1109/IROS.2009.5354199

19. Mahl, T., Mayer, A. E., Hildebrandt, A. & Sawodny, O. A Variable Curvature Modeling Approach for Kinematic Control of Continuum Manipulators. in *American Control Conference* 4945–4950 (2013). doi:10.1109/ACC.2013.6580605

20. Neumann, M. & Burgner-Kahrs, J. Considerations for follow-the-leader motion of extensible tendon-driven continuum robots. in *IEEE International Conference on Robotics and Automation (ICRA)* 917–923 (2016). doi:10.1109/ICRA.2016.7487223

21. Rucker, D. C. & Webster, R. J. Statics and Dynamics of Continuum Robots With General Tendon Routing and External Loading. *IEEE Trans. Robot.* **27,** 1033–1044 (2011).

22. Chen, G., Pham, M. T. & Redarce, T. Sensor-based guidance control of a continuum robot for a semi-autonomous colonoscopy. *Rob. Auton. Syst.* **57,** 712–722 (2009).

23. Conrad, B. L., Jung, J., Penning, R. S. & Zinn, M. R. A Hybrid Continuum-Rigid Manipulation Approach for Robotic Minimally-Invasive Flexible Catheter Based Procedures. (2013).

24. Jones, B. A. & Walker, I. D. Practical Kinematics for Real-Time Implimentation of Continuum Robots. *IEEE Trans. Robot.* 1840–1847 (2006). doi:10.1109/TRO.2006.886268

25. Jones, B. A. & Walker, I. D. Kinematics for multisection continuum robots. *IEEE Trans. Robot.* **22,** 43–55 (2006).

26. Rolf, M. & Steil, J. J. Constant curvature continuum kinematics as fast approximate model for the Bionic Handling Assistant. in *IEEE International Conference on Intelligent Robots and Systems (IROS)* 3440–3446 (2012). doi:10.1109/IROS.2012.6385596

27. Webster, R. J. & Jones, B. A. Design and Kinematic Modeling of Constant Curvature Continuum Robots: A Review. *Int. J. Rob. Res.* **29,** 1661–1683 (2010).

28. Burgner-Kahrs, J., Rucker, D. C. & Choset, H. Continuum Robots for Medical Applications: A Survey. *IEEE Trans. Robot.* **31,** 1261–1280 (2015).

29. Wang, H., Wang, C., Chen, W., Liang, X. & Liu, Y. Three-Dimensional Dynamics for Cable-Driven Soft Manipulator. *IEEE/ASME Trans. Mechatronics* **22,** 18–28 (2017).

30. Jung, J., Penning, R., Ferrier, N. & Zinn, M. R. A Modeling Approach for Continuum Robotic Manipulators : Effects of Nonlinear Internal Device Friction. in *IEEE/RSJ International Conference on Intelligent Robots and Systems*

(IROS) 5139–5146 (2011). doi:10.1109/IROS.2011.6094941

31. Trivedi, D., Lotfi, A. & Rahn, C. D. Geometrically Exact Models for Soft Robotic Manipulators. *IEEE Trans. Robot.* **24,** 773–780 (2008).

32. Sadati, S. M. H. *et al.* A Geometry Deformation Model for Braided Continuum Manipulators. *Front. Robot. AI* **4,** 1–25 (2017).

33. Godage, I. S., Medrano-Cerda, G. A., Branson, D. T., Guglielmino, E. & Caldwell, D. G. Dynamics for variable length multisection continuum arms. *Int. J. Rob. Res.* **35,** 695–722 (2016).

34. Goldman, R. E., Bajo, A. & Simaan, N. Compliant motion control for multisegment continuum robots with actuation force sensing. *IEEE Trans. Robot.* **30,** 890–902 (2014).

35. Renda, F., Cianchetti, M., Abidi, H., Dias, J. & Seneviratne, L. Screw-Based Modeling of Soft Manipulators With Tendon and Fluidic Actuation. *J. Mech. Robot.* **9,** 041012-1 to 041012-8 (2017).

36. Rone, W. S. & Ben-Tzvi, P. Continuum robot dynamics utilizing the principle of virtual power. *IEEE Trans. Robot.* **30,** 275–287 (2014).

37. Marchese, A. D. & Rus, D. Design, kinematics, and control of a soft spatial fluidic elastomer manipulator. *Int. J. Rob. Res.* **35,** 840–869 (2016).

38. Kato, T., Okumura, I., Song, S. E., Golby, A. J. & Hata, N. Tendon-Driven Continuum Robot for Endoscopic Surgery: Preclinical Development and Validation of a Tension Propagation Model. *IEEE/ASME Trans. Mechatronics* **20,** 2252–2263 (2015).

39. Godage, I. S., Branson, D. T., Guglielmino, E., Medrano-Cerda, G. A. & Caldwell, D. G. Shape function-based kinematics and dynamics for variable length continuum robotic arms. in *IEEE International Conference on Robotics and Automation (ICRA)* 452–457 (2011). doi:10.1109/ICRA.2011.5979607

40. Godage, I. S., Guglielmino, E., Branson, D. T., Medrano-Cerda, G. A. & Caldwell, D. G. Novel modal approach for kinematics of multisection continuum arms. in *IEEE/RSJ International Conference on Intelligent Robots and Systems (IROS)* 1093–1098 (2011). doi:10.1109/IROS.2011.6048086

41. Sadati, S. M. H., Naghibi, S., Walker, I. D., Althoefer, K. & Nanayakkara, T. Control Space Reduction and Real-Time Accurate Modeling of Continuum Manipulators Using Ritz and Ritz-Galerkin Methods. *IEEE Robot. Autom. Lett.* **3,** 328–334 (2018).

42. Sadati, S. M. H. *et al.* Mechanics of continuum manipulators, a comparative study of five methods with experiments. in *Towards Autonomous Robotic Systems (TARROS)* 686–702 (Springer International Publishing, 2017). doi:10.1007/978-3-319-64107-2_56

43. Hasanzadeh, S. & Janabi-Sharifi, F. An Efficient Static Analysis of Continuum Robots. *J. Mech. Robot.* **6,** 031011 (2014).

44. Jiang, F., Zhang, H. & Zhao, J. Kinematics and Statics for Soft Continuum Manipulators With Heterogeneous Soft Materials. in *ASME Dynamic Systems and Control Conference* (2016). doi:10.1115/DSCC2016-9909

45. Shapiro, Y., Gabor, K. & Wolf, A. Modeling a Hyperflexible Planar Bending Actuator as an Inextensible Euler–Bernoulli Beam for Use in Flexible Robots. *Soft Robot.* **2,** 71–79 (2015).

46. Rucker, D. C. & Webster, R. J. Deflection-Based Force Sensing for Continuum Robots: A Probabalistic Approach. in *IEEE/RSJ International Conference on Intelligent Robots and Systems (IROS)* 3764–3769 (2011). doi:10.1109/IROS.2011.6094526

47. Alici, G., Canty, T., Mutlu, R., Hu, W. & Sencadas, V. Modeling and Experimental Evaluation of Bending Behavior of Soft Pneumatic Actuators Made of Discrete Actuation Chambers. *Soft Robot.* **5,** 24–35 (2018).

48. Fraś, J., Czarnowski, J., Maciaś, M. & Główka, J. Static modeling of multisection soft continuum manipulator for stiff-flop project. *Adv. Intell. Syst. Comput.* **267,** 365–375 (2014).

49. Kang, R., Guo, Y., Chen, L., Branson, D. T. & Dai, J. S. Design of a Pneumatic Muscle Based Continuum Robot With Embedded Tendons. *IEEE/ASME Trans. Mechatronics* **22,** 751–761 (2017).

50. Dehghani, M. & Moosavian, S. A. A. Compact modeling of spatial continuum robotic arms towards real-time control. *Adv. Robot.* **28,** 15–26 (2014).

51. Falkenhahn, V., Mahl, T., Hildebrandt, A. & Sawodny, O. Dynamic Modeling of Bellows-Actuated Continuum Robots Using the Euler – Lagrange Formalism. *IEEE Trans. Robot.* **31,** 1483–1496 (2015).

52. Amanov, E., Granna, J., Member, S. & Burgner-kahrs, J. Toward Improving Path Following Motion: Hybrid

Continuum Robot Design. in *IEEE International Conference on Robotics and Automation (ICRA)* 4666–4672 (2017). doi:10.1109/ICRA.2017.7989542

53. Cowan, L. S. & Walker, I. D. The importance of continuous and discrete elements in continuum robots. *Int. J. Adv. Robot. Syst.* **10,** (2013).

54. Giri, N. & Walker, I. D. Three module lumped element model of a continuum arm section. in *IEEE/RSJ International Conference on Intelligent Robots and Systems (IROS)* 4060–4065 (2011). doi:10.1109/IROS.2011.6048577

55. Godage, I. S., Wirz, R., Walker, I. D. & Webster, R. J. Accurate and Efficient Dynamics for Variable-Length Continuum Arms: A Center of Gravity Approach. *Soft Robot.* **2,** 96–106 (2015).

56. Duriez, C. & Bieze, T. Soft Robot Modeling, Simulation and Control in Real-Time. **17,** 103–109 (2017).

57. Bieze, T. M. *et al.* Finite Element Method-Based Kinematics and Closed-Loop Control of Soft, Continuum Manipulators. *Soft Robot.* **00,** (2018).

58. Gazzola, M., Dudte, L. H., McCormick, A. G. & Mahadevan, L. Forward and inverse problems in the mechanics of soft filaments. *R. Soc. Open Sci.* **5,** (2018).

59. Duriez, C. Control of elastic soft robots based on real-time finite element method. in *IEEE International Conference on Robotics and Automation* 3982–3987 (2013). doi:10.1109/ICRA.2013.6631138

60. Tunay, I. Spatial continuum models of rods undergoing large deformation and inflation. *IEEE Trans. Robot.* **29,** 297–307 (2013).

61. He, B., Wang, Z., Li, Q., Xie, H. & Shen, R. An analytic method for the kinematics and dynamics of a multiple-backbone continuum robot. *Int. J. Adv. Robot. Syst.* **10,** (2013).

62. Santina, C. Della, Lakatos, D., Bicchi, A. & Albu-schaeffer, A. Using Nonlinear Normal Modes for Execution of Efficient Cyclic Motions in Soft Using Nonlinear Normal Modes for Execution of Efficient Cyclic Motions in Soft Robots. 1–17 (2018).

63. Lock, J., Laing, G., Mahvash, M. & Dupont, P. E. Quasistatic modeling of concentric tube robots with external loads. in *IEEE/RSJ International Conference on Intelligent Robots and Systems (IROS)* 2325–2332 (2010). doi:10.1109/IROS.2010.5651240

64. Xu, K. & Simaan, N. An investigation of the intrinsic force sensing capabilities of continuum robots. *IEEE Trans. Robot.* **23,** 576–587 (2008).

65. Blanc, L., Delchambre, A. & Lambert, P. Flexible Medical Devices: Review of Controllable Stiffness Solutions. *Actuators* **6,** 1–31 (2017).

66. Vitiello, V., Lee, S.-L., Cundy, T. P. & Yang, G. Z. Emerging Robotic Platforms for Minimally Invasive Surgery. *IEEE Rev. Biomed. Eng.* **6,** 111–126 (2013).

67. Bajo, A., Pickens, R. B., Herrell, S. D. & Simaan, N. Constrained motion control of multisegment continuum robots for transurethral bladder resection and surveillance. in *IEEE International Conference on Robotics and Automation (ICRA)* 5837–5842 (2013). doi:10.1109/ICRA.2013.6631417

68. Cianchetti, M. & Laschi, C. Pleasant to the Touch: By Emulating Nature, Scientists Hope to Find Innovative New Uses for Soft Robotics in Health-Care Technology. *IEEE Pulse* **7,** 34–37 (2016).

69. Dometios, A. C., Papageorgiou, X. S., Arvanitakis, A., Tzafestas, C. S. & Maragos, P. Real-Time Dynamical Trajectory Tracking Using Online Point-Cloud Data : Towards a User Adaptive Assistive Bath Robot. in *IEEE/RSJ International Conference on Intelligent Robots and Systems (IROS)* 5031–5036 (2017).

70. Manti, M. *et al.* Exploiting Morphology of a Soft Manipulator for Assistive Tasks. in *Springer-Verlag* **8064,** (2011).

71. Bajo, A. & Simaan, N. Hybrid motion/force control of multi-backbone continuum robots. *Int. J. Rob. Res.* **35,** 422–434 (2016).

72. Godage, I. S., Branson, D. T., Guglielmino, E. & Caldwell, D. G. Path planning for multisection continuum arms. in *IEEE International Conference on Mechatronics and Automation (ICMA)* 1208–1213 (2012). doi:10.1109/ICMA.2012.6283423

73. Calisti, M. *et al.* An octopus-bioinspired solution to movement and manipulation for soft robots. *Bioinspiration and Biomimetics* **6,** (2011).

74. Cianchetti, M. *et al.* STIFF-FLOP surgical manipulator: Mechanical design and experimental characterization of the single module. in *IEEE/RSJ International Conference on Intelligent Robots and Systems (IROS)* 3576–3581 (2013). doi:10.1109/IROS.2013.6696866

75. Xu, K. & Simaan, N. Analytic Formulation for Kinematics, Statics, and Shape Restoration of Multibackbone Continuum Robots Via Elliptic Integrals. *J. Mech. Robot.* **2,** 011006 (2010).

76. Back, J., Lindenroth, L., Karim, R., Althoefer, K. & Rhode, K. New Kinematic Multi - Section Model for Catheter Contact Force Estimation and Steering. in *IEEE/RSJ International Conference on Intelligent Robots and Systems (IROS)* 2122–2127 (2016). doi:10.1109/IROS.2016.7759333

77. Kim, S., Laschi, C. & Trimmer, B. Soft robotics: A bioinspired evolution in robotics. *Trends Biotechnol.* **31,** 287–294 (2013).

78. Polygerinos, P. *et al.* Soft Robotics: Review of Fluid-Driven Intrinsically Soft Devices; Manufacturing, Sensing, Control, and Applications in Human-Robot Interaction. *Adv. Eng. Mater.* 1–22 (2017). doi:10.1002/adem.201700016

79. Ranzani, T., Cianchetti, M., Gerboni, G., DeFalco, I. & Menciassi, A. A Soft Modular Manipulator for Minimally Invasive Surgery: Design and Characterization of a Single Module. *IEEE Trans. Robot.* **32,** 187–200 (2016).

80. Liu, W. & Rahn, C. D. Fiber-Reinforced Membrane Models of McKibben Actuators. *J. Appl. Mech.* **70,** 853 (2003).

81. Akamatsu, Y., Nakamura, T. & Kusaka, Y. Development of a soft manipulator with flexible joints using smart fluid and pneumatics cushion for collision with human. in *IEEE/ASME International Conference on Advanced Intelligent Mechatronics, AIM* 1–6 (2007). doi:10.1109/AIM.2007.4412487

82. Shiva, A. *et al.* Tendon-Based Stiffening for a Pneumatically Actuated Soft Manipulator. *IEEE Robot. Autom. Lett.* **1,** 632–637 (2016).

83. Gent, A. N. *Engineering with Rubber - How to Design Rubber Components*. *Carl Hanser Verlag* (2012). doi:10.5254/1.3538214

84. Puglisi, G. & Saccomandi, G. The Gent model for rubber-like materials: An appraisal for an ingenious and simple idea. *Int. J. Non. Linear. Mech.* **68,** 17–27 (2015).

85. Horgan, C. O. The remarkable Gent constitutive model for hyperelastic materials. *Int. J. Non. Linear. Mech.* **68,** 9–16 (2015).

86. Hopcroft, M. a, Nix, W. D. & Kenny, T. W. What is the Young ' s Modulus of Silicon ? *J. Microelctromechanical Syst.* **19,** 229–238 (2010).

A. APPENDIX 1

Longitudinal engineering stress for a braided extensor as a function of elongation λ and braiding angle γ; for the Gent model with INF constraint:

$$\sigma = \frac{GJ_m \ln\left(\frac{\frac{\lambda^2 C_\gamma^2 - 1}{S_\gamma^2} - \lambda^2 + \frac{S_\gamma^2}{\lambda^2\left(\lambda^2 C_\gamma^2 - 1\right)} + 3}{J_m} + 1\right) C_\gamma^2 S_\gamma^2}{\left(1 - \lambda^2 C_\gamma^2\right)^2} + \frac{GS_\gamma^2\left(2\lambda - \frac{2\lambda C_\gamma^2}{S_\gamma^2} + \frac{2S_\gamma^2}{\lambda^3\left(\lambda^2 C_\gamma^2 - 1\right)} + \frac{2C_\gamma^2 S_\gamma^2}{\lambda\left(\lambda^2 C_\gamma^2 - 1\right)^2}\right)}{2\lambda\left(\frac{\frac{\lambda^2 C_\gamma^2 - 1}{S_\gamma^2} - \lambda^2 + \frac{S_\gamma^2}{\lambda^2\left(\lambda^2 C_\gamma^2 - 1\right)} + 3}{J_m} + 1\right)\left(1 - \lambda^2 C_\gamma^2\right)} + \frac{GJ_m \ln\left(\frac{\frac{\lambda^2 C_\gamma^2 - 1}{S_\gamma^2} - \lambda^2 + \frac{S_\gamma^2}{\lambda^2\left(\lambda^2 C_\gamma^2 - 1\right)} + 3}{J_m} + 1\right) S_\gamma^2}{2\lambda^2\left(1 - \lambda^2 C_\gamma^2\right)}$$

B. APPENDIX 2

An alternate approach can be formulated for constructing the transformation matrices. As the total local moment is calculated as: $\boldsymbol{M}_{tot} = \boldsymbol{M}_e + \boldsymbol{M}_i$, projecting this moment vector onto its local x and y components delivers curvature in the local frame as $\kappa_x = M_y/EI$ and $\kappa_y = M_x/EI$, with:

$\kappa = \sqrt{\left(\kappa_x^2 + \kappa_y^2\right)}$; and the out of plane bending angle as: $\varphi = atan2(\kappa_y/\kappa_x)$ [27].

Observing that $\boldsymbol{\rho} = [(1 - C_\theta)/\kappa \ , 0 \ , \ S_\theta/\kappa]^T$ as the translational vector from the previous frame to next due to bending between two incrementally adjacent frames is derived as [27]:

$$\boldsymbol{T}_b = \begin{bmatrix} \boldsymbol{R}_z(\varphi) & \boldsymbol{0} \\ \boldsymbol{0}^T & 1 \end{bmatrix} . \begin{bmatrix} \boldsymbol{R}_y(\theta) & \boldsymbol{\rho} \\ \boldsymbol{0}^T & 1 \end{bmatrix} . \begin{bmatrix} \boldsymbol{R}_z(-\varphi) & \boldsymbol{0} \\ \boldsymbol{0}^T & 1 \end{bmatrix} \tag{20}$$

where $\boldsymbol{R}_{3\times3}$ is the rotational transformation matrix around the relevant local axis.

The torsion angle is computed as: $\alpha = M_z\xi_0/GI_p$,where I_p is the polar moment of inertia. This could be represented by a local rotational transformation about the z axes by the angle α in the following transformation matrix:

$$\boldsymbol{T}_{tor_z} = \begin{bmatrix} \boldsymbol{R}_z(\alpha) & \boldsymbol{0} \\ \boldsymbol{0}^T & 1 \end{bmatrix} \tag{21}$$

By considering each infinitesimal segment as a beam, the shear displacement in each local frame for both x and y directions are calculated as:

$$\delta_{x,y} = (f_{x,y}\xi_0/\beta AG) \tag{22}$$

where $f_{x,y}$ is the force projection of the resultant overall local force on the local x, y plane, and β is the form factor calculated by $(A/I^2)\int_A \frac{Q}{t} dA$ which is $10/9$ for circular cross sections. Therefore, the resulting shear translational vector in both the local x and y directions is: $\boldsymbol{\varrho}_{x,y} = \left[-\delta_x \ , -\delta_y \ , 0 \ \right]^T$, forming the shear transformation matrix as:

$$\boldsymbol{T}_{sh_{x,y}} = \begin{bmatrix} \boldsymbol{I}_{3\times3} & \boldsymbol{\varrho}_{x,y} \\ \boldsymbol{0}^T & 1 \end{bmatrix} \tag{23}$$

where $\boldsymbol{I}_{3\times3}$ is the identity matrix. The total homogenous transformation matrix from one frame to the next is composed as a concatenation of all calculated homogenous matrices:

$$\boldsymbol{T}_k^{k-1}{}_{tot} = \boldsymbol{T}_b\boldsymbol{T}_{sh}\boldsymbol{T}_{tor} \tag{24}$$

The relative coordinates of every following frame are the first three entries of the last column in each transformation matrix; which we stack successively in a separate $3 \times n$ matrix.
The overall transformation matrix from the tip to the base is formed as a multiplication of all transformations:

$$\boldsymbol{T}_n^0 = \left(\prod_{n-1}^{0} \boldsymbol{T}_{tot}\right)\boldsymbol{T}_n^{n-1} \tag{25}$$

By this approach, using an appropriate level of discretization, the system's nonlinear deformation is captured by geometrical nonlinearity as a result of high number of segments, rather than the material nonlinearity by considering more complex hyperelastic assumptions.

Comparison with the results obtained from the method described in the text shows a minor difference of about 2% between the two methods in the current robotics appendage with discretized in 100 sections.

C. APPENDIX 3

Although rubber is capable of experiencing large elastic deformations, in practice rubber is often subjected to only to relatively less than about 50% in extension or compression (small strains). The stress can then be approximated by common elastic analysis, assuming simple linear stress-strain relationships, since in small strains, rubber behaves as a linearly-elastic material like all solids [83]. In other to further investigate the validity of Hooke linear relation for the material used in the soft robot appendage, one chamber (braided extensor) was separated and pressurized to an elongation of almost over 87% more than its initial length. Results are depicted in Fig.19., showing the elongation to follow a nearly linear trend.

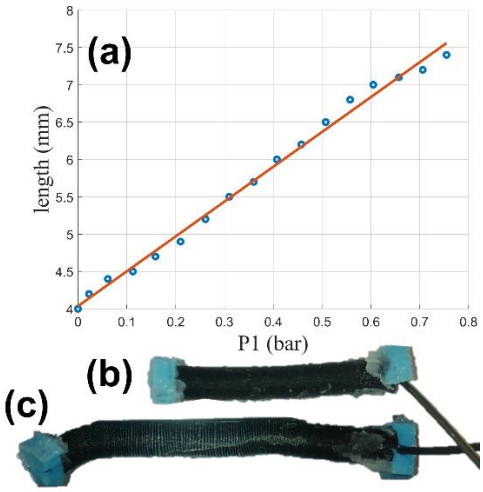

Fig.19: Pressurization of a braided extensor: (a) Pressure vs. length, (b) initial configuration, (c) elongated extensor.